UNIVERSITY OF CALIFORNIA
RIVERSIDE

Long Distance Non-Line-of-Sight Ultraviolet Communication Channel Analysis and Experimental Verification

A Dissertation submitted in partial satisfaction
of the requirements for the degree of

Doctor of Philosophy

in

Electrical Engineering

by

Linchao Liao

December 2015

Dissertation Committee:

Dr. Gang Chen, Co-Chairperson
Dr. Albert Wang, Co-Chairperson
Dr. Qi Zhu

The Dissertation of Linchao Liao is approved:

Committee Co-Chairperson

Committee Co-Chairperson

University of California, Riverside

Acknowledgments

I am deeply grateful my advisor, Dr. Gang Chen, for his guidance, patient advising, understanding and continuous support. He guided me through my Ph.D. research by sharing his enthusiasm, knowledge and experience with me. I would also like to heartily express my greatest appreciation to Dr. Albert Wang, for his continuous guidance, help and support. I also would like to thank the Department of Electrical Engineering at UC Riverside, especially the members of my dissertation committee, Dr. Qi Zhu, for his valuable inputs, discussions and feedbacks on my research.

I had the pleasure of working closely with team members in WITLAB. I am grateful to the friendship of all members of the research group: Qunfeng He, Kaiyun Cui, Samuel Ibarra, Qian Gao, Tian Lang, and Zening Li.

My research and life at UC Riverside have been enriched by my best friends, Peng Deng, Panruo Wu, and Zening Li. With them, my research and life at UCR is never boring. We shared ideas, experiences and opinions not only in life, but also in research. I'm so fortunate to have them in UCR.

Most important of all are my families' support and love. In the past four and half years, my parents suffered in a unthinkable living way without their only child by the side. When I was away from home, they held me from anything that might be concerning and distracting. In some of the occasions when they needed me most, I was not able to make it unfortunately. Their love and support are unselfish, pure and persistent. I know I'm living their best wishes and expectations. I'm doing every means not to let them down. My wife, Xuan Sun is the best gift I can have in my life. All through these years, we lived in

different countries separately and only can see each other through Wechat. This is what I feel afflicted and so regretted with. Her pure and kind personality is what drives me to be a better man. For my families' unconditional love and care, I dedicate this thesis to them.

At last, I need to point out that partial data in chapter 3 and all the experiment data in chapter 4 can be found from my previous published journal two paper: "Linchao Liao, Robert J. Drost, Zening Li, Tian Lang, Brain. M. Sadler and Gang Chen, Long-distance non-line-of-sight ultraviolet communication channel analysis: experimentation and modelling IET Optoelectronics, Volume 9, Issue 5, October 2015, p. 223-231" and "Linchao Liao, Zening Li, Tian Lang, and Gang Chen, "UV LED array based NLOS UV turbulence channel modeling and experimental verification," Opt. Express23, 21825-21835 (2015)".

To my parents for all the support.

ABSTRACT OF THE DISSERTATION

Long Distance Non-Line-of-Sight Ultraviolet Communication Channel Analysis and Experimental Verification

by

Linchao Liao

Doctor of Philosophy, Graduate Program in Electrical Engineering
University of California, Riverside, December 2015
Dr. Gang Chen, Co-Chairperson
Dr. Albert Wang, Co-Chairperson

In this thesis, the characteristics of long-distance non-line-of-sight (NLOS) ultraviolet (UV) communication channel are studied through experiment and theoretical analysis. The research focuses on the validation of different channel models, long distance NLOS link loss and received signal energy distribution based on outdoor experiment results and numerous simulations. All the previous research on NLOS UV only considered short communication range scenarios, in which turbulence effects were assumed to be negligible. In fact, with the increasing of communication distance, optical turbulence effects may degrade UV communication performance because the fading irradiance significantly deteriorates the received signal in two aspects: received energy fluctuation and extra path loss.

In the beginning, the author conducts a comprehensive outdoor channel measurement experiment from several hundreds meters up to four thousand meters. To the best of our knowledge, this experiment represents the most comprehensive examination of the NLOS UV communication channel at such distances. By reporting experimentally collected

data, we illustrate two approaches to measuring path loss. In addition to highlighting practical issues, which is death time, that must be considered when performing such measurements, the data provide validation of a previously reported Monte Carlo multiple-scattering channel model. In addition, we examine the distribution of received photon counts for evidence of the effects of turbulence in the NLOS channel. In this case, however, there is less agreement with predictions from existing turbulence models, suggesting the need for additional research on the refinement of turbulence modeling.

For this reason, we then propose a MC channel model to capture the multiple scattering channel behavior under turbulence condition. In addition, we present a serial experimental results and study the characteristic of NLOS UV turbulence channel with farthest distances up to 1 km. Through the experiment and simulation, we discuss the turbulence effect on NLOS UV channel with focus on received-signal energy distribution and channel path loss. What's more, a special characteristic of NLOS UV channel is proposed and studied as well, which is turbulence strength trade off between path length and common volume size. This is the first experiment to study NLOS UV turbulence channel characteristic. These experimental and simulated results are valuable for studying NLOS UV channel and communication system design.

Contents

List of Figures

List of Tables

Chapter 1

Introduction

1.1 Background of Optical Wireless Communication and Ultraviolet Communication

During human being's history, wireless communication is always one of most important and fastest developing area. Date back to thousands years ago, roman people have already used tools to make a loud sound to inform their army in the battle field. Chinese people made used of the smoke signal to communicate between each station on the great wall to notice enemy's invasion and flashing lights have been used to transmit information between warships at sea since the days of Lord Nelson. In past two hundred years, with the developing of radio frequency (RF) communication, human being's society has been totally reformed, e.g., it makes it possible that one can talk to his friend on the other side of earth; it makes your mobile devices can receive data from satellite or radio base station. However, as the increasing of people's demand, RF communication gradually cannot meet

the requirement due to the limited bandwidth, data rate and its broadcasting property.

By using light to send information is not a brand new idea, because our ancient have taken advantage of it. In past few decades, people put more attention and effort on optical wireless communication (OWC) and consider it as an alternative way to RF communication. Compared to RF communication, OWC has its own advantages, such as huge unlicensed bandwidth, weight and size of its device, low material cost, no electromagnetic interference, potential increase of data rate and better security. There are three majority kinds of optical wireless communication: infrared (IR) communication, visible light communication (VLC) and ultraviolet (UV) communication. And their wavelength ranges are depicted in Fig. 1.1.

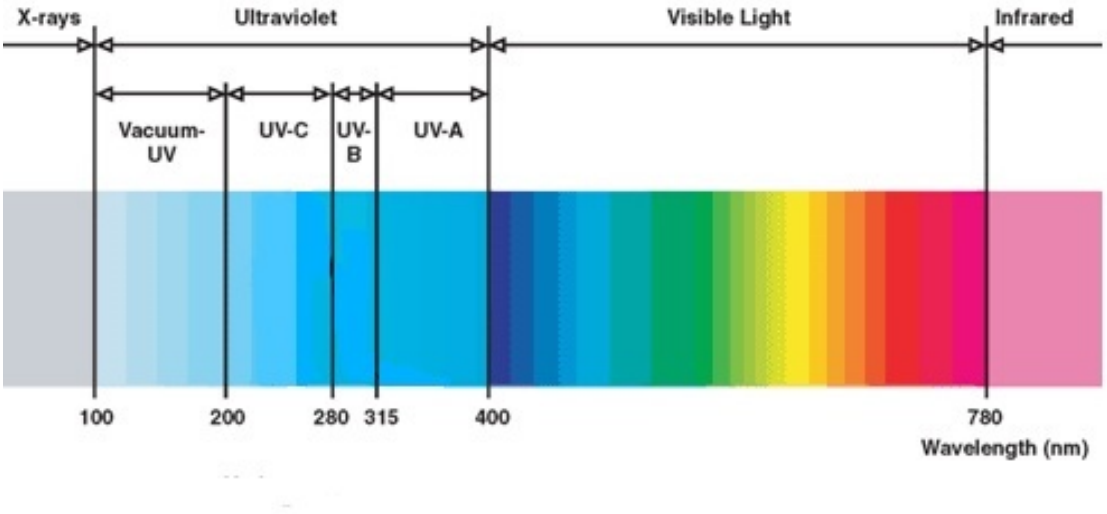

Figure 1.1: Optical spectrum illustration.

In general, OWC geometry configuration could be classified into two aspects: line-of-sight (LOS) and non-line-of-sight (NLOS). LOS scenario is straightforward, which indicates the transmitter is pointed towards the receiver aperture. It can be also referred as free-space optical (FSO) communication. Due to some unique channel characteristics, N-LOS geometry configuration can also be achieved to transmit information that is what this thesis focus on. A typical optical wireless link system is similar to a RF communication link, which is composed of a information source, modulator, communication channel, demodulator, and receiver. In what follows, we firstly introduce the key system components of a OWC link, such as the source, photon detector, modulation scheme, channel characteristic. Then we elaborate the motivations of the research, relevant previous work and the major contributions of this thesis.

1.1.1 UV Transmitter Characteristics

Light source is always a key element in any optical wireless communication system. Such a device should not only produce energy concentrated in a narrow wavelength band, but also can be easily modulated. The most command light source until now are the light-emitting diodes (LED), the laser, and the laser diodes (LD). In addition to those three, in early days, mercury lamp was also employed as source which has moderately high optical power, but it's fragile and sensitive to temperature variation. What's worse it requires high power consumption and with low modulation rate and short using lifetime. There is also a light source called solid state laser, which can produce high peak optical power and narrow spectral width with a narrow beam angle. However, UV solid state laser is relatively expensive, power consumption, large size and requires a optical lens on top to diverge beam

if wide beam angle angle is needed.

The most important communication characteristics of any optical source are its modulation bandwidth, input-output power curve, frequency spectrum and spectrum purity. The spreading of spectrum around the desired wavelength indicates the presence of unwanted frequencies, or undesired noise modulations, superimposed on the output wavelength. This sprectral spreading can hinder the ability to recognize desired information modulated on the source. Light-emitting diodes have relatively wide spectral extent (hundreds of Angstroms), whereas laser significantly improve the light purity.

Thanks to DARPA SUVOS program laughed in 2002, a variety of UV LED sources are commercially available since then. These LEDs require low power consumption, but can support up to 50 Mhz modulation bandwidth. However, its average optical power and power efficiency are low. But, the output optical power issue can be increased by using a LED array, which can provide enough optical power for our experiment within 1km. Light-emitting diodes have low thresholds and can operate at low-current values, but they have limited peak powers. Laser diodes require more drive current, but have higher peak power. Laser tubes generally have to be pumped above threshold and are difficult to stabilize in the linear rage. Therefore, high-power lasers are usually operated as continuous-wave devices at their peak power capability. As the baseline distance increase, a UV laser has to be employed for longer distance. In this thesis, all the experiment and simulation are based on UV LED array or UV laser.

1.1.2 UV Receiver Characteristics

Photodetection of light field represents the key operation in the optical receiver, converting the collected field to a current or voltage waveform for subsequent post-detection processing. There are two basic practical photodetectors: photomultiplier (PMT) and avalanche photodiode (APD). A PMT is a phototube with multiple plates (dynodes) that each produce sencondary emissions, thereby multiplying up the current flow. Because secondary emissions can be made extremely high, a PMT can have mean gains in the 10^3 to 10^5 range. The gain variance is often described by a spreading factor ξ. The avalanche photodiode (APD) is a solid-state diode with junction material providing current gain by repeated electron ionization. An APD can provide mean gain values in the range of 50 to 300 times. A complete theory of avalanching mechanism has been developed, and fairly reliable gain statistics can be modeled for the APD.

The PMT characteristics of high sensitity and low noise make it pretty suitable for implementing a photon counting receiver which counts the incoming number of photons for signal and noise before decision, during the process of which Poisson distribution is a natural reaction. This is a fundamental premise for the theoretical study within the framework of Poisson communication theory. Similar to PMT, the inherent amplification process is statistically random and output photocurrent thus experiences variations, the effect of which is defined as so-called APD excess noise. As a silicon based photodiode, APD reacts much faster than PMT does but produces much more noise. The fact leads to the treatment of the noise as the thermal white Gaussian noise.

1.1.3 UV Communication Channel Characteristics

Infrared communication (IR) are well studied and already applied into many areas, such as distant measurement and Infrared Data Association (IrDA), which has been embedded into many laptops and cell phones. Visible light communication (VLC) is also very promising on many applications: indoor LiFi, traffic light communication and smart home control etc.

However, both infrared and visible light have their drawbacks. Infrared restricts to Line-Of-Sight (LOS) too much and visible light has to conquer huge interference from intense solar background noise. Fortunately, UV-C (ranges from 200nm to 280 nm) can overcome those restrictions with its special characteristics. First, UV-C is "solar blind"[1]. After through atmosphere, the solar radiation relatively keeps its longer wave and loses the shorter wave instead. Large attenuation of UV band is observed, which makes solar radiation in the UV-C band to be negligible[2]. By operating in this region, a ground-based photon detector can exploit the low background noise, unlike visible light and infrared. This characteristic makes it possible that developing wide Field-Of-View (FOV) aperture to receive more energy without much noise. Second, the wavelength of UV-C is the same size order as the molecular in the air, which will cause strong scattering. As long as a certain number of photons sent by a transmitter arrive at a receiver, a communication link can be established[3]. This characteristic makes communication in UV-C band survive in Non-Line-Of-Sight (NLOS) path and relaxes the strict requirement on pointing, acquisition and tracking (PAT). In addition, UV-C signals are inherently jamming-resistant and not easy to be intercepted when signal beyond the extinction range. With above great advantages,

the NLOS UV communication becomes promising and suitable for civilian and military application[4], such as environment sensing, unattended ground sensor networks, inter-soldier communication and UV guided automatic landing on aircraft carrier (shown in below Fig.1.2 and Fig. 1.3).

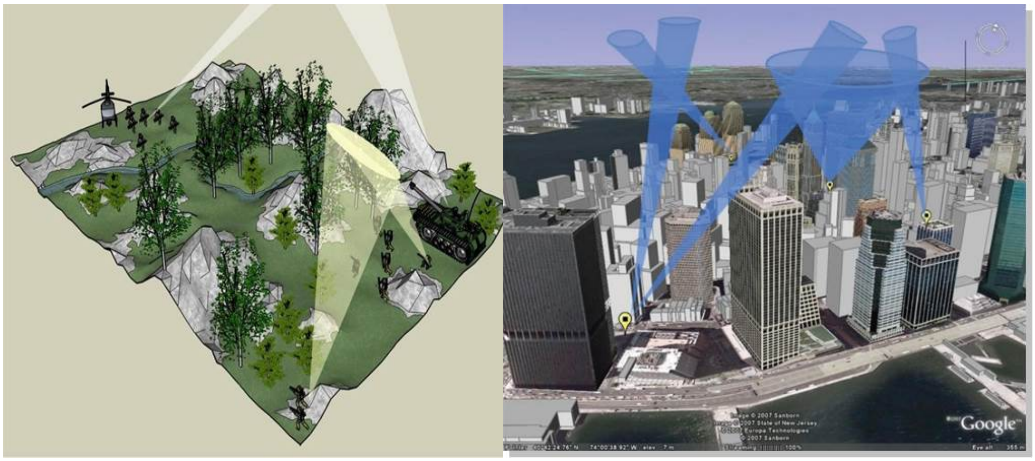

Figure 1.2: UV for civilian use.

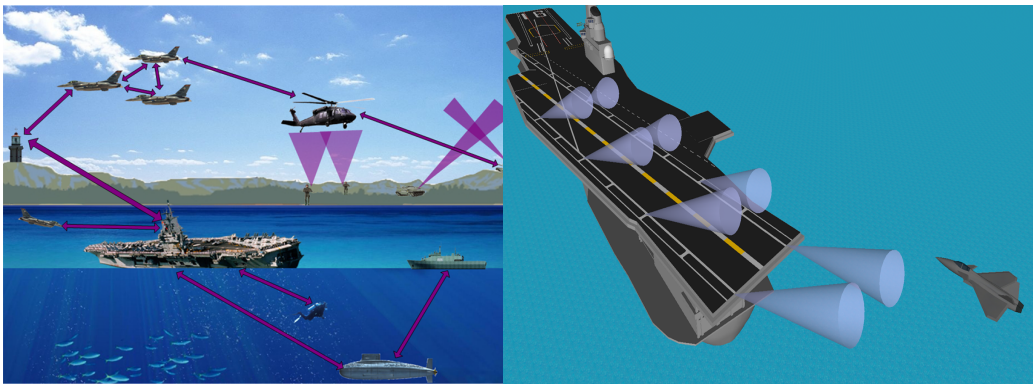

Figure 1.3: UV for military use.

As such, in the past few years, ultraviolet communication becomes more and more popular, due to its special characteristic[5] and it has potential for low data-rate appli-

cations, supplementing or replacing conventional radio-frequency (RF) systems when RF communication is not allowed or undesirable.

1.1.4 Modulation Scheme

The overall system may be designed as a direct detection (incoherent) system in which intensity modulation (IM) is used, or can be a coherent system with direct optical carrier modulation. At the receiver side, the field is photodetected (by direct detection or by heterodyning) and the output current is processed to determine the transmitted bit during each bit interval. Since the encoding operation is known at the receiver, a correct bit decision can be made by deciding which of the two optical fields was received. The resulting sequence of decoded bits then represents the received version of the transmitted bits. Hence, accurate bit transmission is directly related to the ability to identify the photodetected optical field. Background noise, in-out noise fields, and detector noise incurred during photodetection, will cause decoding bit errors, degrading the digital performance. Thus the probability that any given bit will be decoded in error (bit error probability) becomes an important performance measure in digital systems.

The most common forms of pulsed modulation scheme in binary direct detection receivers are on-off keying (OOK) and pulse-position modulation (PPM). In OOK, each bit is transmitted by either pulsing the light source on or off during each bit time. This represents the most basic type of optical signaling and corresponds to merely blinking the light sourcr for digital encoding. Pulse-position modulation (PPM) is a form of signal modulation in which M message bits are encoded by transmitting a single pulse in one of possible required time-shifts. This is repeated every T seconds, such that the transmitted

bit rate is bits per second.

1.2 Motivation and Progress of NLOS UV Communication

Extensive research work have been performed, not only experimentally, but also theoretically on NLOS UV communication. Under the assumption of single scattering, analytical and tractable single scattering channel path loss models have been developed in [1][5]. Through a short range outdoor experiment, an empirical path loss model has been proposed in [6] and it also partially validated the correctness of single scattering channel path loss model. In [7][8], authors proposed a numerical multiple scattering channel path loss model based on Monte Carlo method (MC). After the verification of [9], this MC based multiple scattering model was shown to be more accurate than single scattering channel path loss model. Under the assumptions of those two path loss models, NLOS UV channel coding [10], modulation schemes [11], NLOS UV MAC, and network issues [12],[13],[14] have been also studied and discussed. Meanwhile, practical communication systems were built [15],[16] for experimentation and validation of theoretical NLOS UV communication research.

However, these works only considered short communication range scenarios, in which turbulence effects were assumed to be negligible. In fact, as communication range and the index of refraction structure parameter increase, optical turbulence in the UV-C band may deteriorate the communication system performance with the effects of irradiance fluctuation (scintillation) and extra signal attenuation. Thus, author in [17] proposed an analytical model of NLOS UV turbulence channel for the first time. In paper [18],[19],

authors advanced the previous model and took extra turbulence attenuation into account. Both of those two models, however, were limited because they assumed that the photons were only scattered once before detected by the receiver.

Therefore, in order to obtain a more clear understanding of long distance NLOS UV channel, we propose a series of comprehensive procedures to character communication channel. Combining experiment and simulation, we aim to achieve a thorough vision of long distance NLOS UV channel, which is the prime of system and MAC design.

1.3 Contributions and Outline of the Thesis

Our study of NLOS UV communications is built on the experimental investigation and modeling of the communication channel. This thesis consists of six chapters and the rest chapters are organized as follows:

Chapter 2 introduces the fundamental concepts of NLOS UV communication and some basic channel models. And then the author describes a basic UV channel test bed and some initial experiment results, from which some practical issues during the experiment are found and discussed further.

Chapter 3 reports on a first hand data collection experiment in which a variety of channel-sounding measurements were taken to characterize various aspects of long-distance NLOS UV communications. In particular, analyses of measurements of path loss, pulse broadening, and photon-count distributions were presented and compared with previously developed theoretical channel models. Predictions from a Monte Carlo propagation model are in reasonable agreement with several of the experimental measurements, providing

validation of this modeling approach. However, the path loss measurements do exhibit mismatch with this channel model, which generally under predicts the observed path loss. This mismatch might be attributable in part to tolerances in device specifications, but other possible sources of additional channel attenuation should be considered. For example, we presented path loss estimates incorporating turbulence-induced attenuation (as predicted by previously developed turbulence modeling) that exhibit reduced error with respect to the path loss measurements. However, model predictions of other turbulence effects, such as a log-normal distribution of received photon counts, do not appear to be supported by the experimental data, suggesting the need for model refinement. Using the experimental path loss measurements, we also considered the BER performance of a representative long-distance NLOS UV communication system.

Chapter 4 investigates NLOS UV turbulence channel for the first time by conducting a series of measurements. The received-signal distributions and NLOS UV turbulence channel path losses are studied in terms of system geometry and turbulence strength. The comparison between experimental and simulated results provided the validation for the NLOS UV turbulence channel model based on MC method. Through field test data and simulation results, the received-signal energy is proved to follow LN distribution in NLOS scenarios when the pointing angles are low and the atmosphere is in weak-medium turbulence condition. In addition, we also prove that turbulence effect will induce extra path loss for NLOS UV communication. The special characteristic of NLOS UV channel was also observed and analyzed through experiment and simulation. Because of this special characteristic, the choice of system geometry becomes a trade off between the size of common

volume and channel length.

Chapter 5 presents a NLOS UV communicatoin system based on USRP, and then, author compared practical system performance to three previous proposed path loss models and BER models. All discrepancies are analyzed, which are valuable for NLOS UV communication system design. What's more, We were also able to verify the basic operation of both our protocols. From the results, we are able to see that a node is able to react accordingly to the information it receives. The nodes were able to find each other during the neighbor discovery process. They were able to obtain the address of its neighbor and the direction it could use to communicate with it. Once a node contained this information, the MAC protocol was used to exchange information.

Chapter 6 highlights the contents of the thesis and the major conclusions.

Chapter 2

Fundamentals of NLOS UV communication and practical issues of experiment

2.1 Introduction

Channel modeling for NLOS UV communication is the fundamental for system and network design, as well as performance analysis. In this chapter, we first introduce some basic concepts of NLOS UV channel characteristics and some basic channel path loss models. And then, we present a outdoor experiment and some initial results, from which we can find out some practical issues during the experiment.

2.2 Fundamentals of NLOS UV Communication Channel Model

A typical NLOS UV communication geometry illustrated by [20], as shown in Fig. 2.1. The transmitter and receiver are coplanar. Denote the Tx beam full-width divergence by ϕ_1, the Rx FOV angle by ϕ_2, the tx pointing angle by θ_1, Rx pointing angle by θ_2, the Tx and Rx baseline separation by r, and the distances of the common volume V to the Tx and Rx by r_1 and r_2, respectively. Also, θ_s is the angle between the forward direction of incident waves and the observation direction.

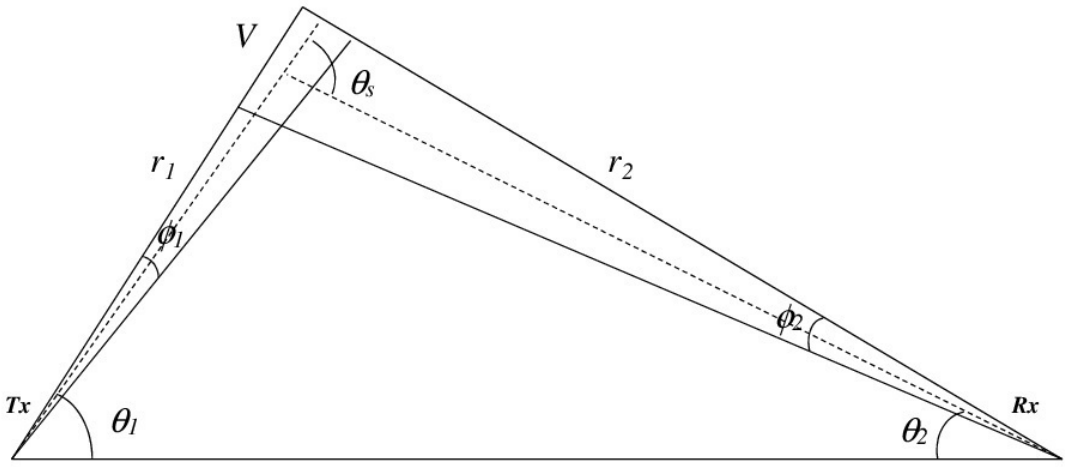

Figure 2.1: UV NLOS communication link geometry.

In NLOS UV communication, special channel case, scattering and absorption are two dominate factors. We assume a homogeneous atmosphere and use the following coefficients: the Rayleigh (molecular) scattering coefficient k_s^{Ray}, Mie (aerosol) scattering coefficient k_s^{Mie}, absorption coefficient k_a, and extinction k_e. [21]The total scattering co-

efficient is defined as the sum of the two scattering coefficient $k_s = k_s^{Ray} + k_s^{Mie}$, and the extinction coefficient is given by the sum of the scattering and absorption coefficient as $k_e = k_s + k_a$[22]. We roughly consider atmosphere condition for four cases: typical tenuous, thick, extra thick (corresponding to clear, overcast, foggy, dense foggy) given in Table 1. All our experiments are considered to be conducted under thick plus condition.

Table 2.1: Atmosphere model parameter: tenuous, thick and extra thick conditions.

atmosphere	$k_s^{Ray}(km^{-1})$	$k_s^{Mie}(km^{-1})$	$k_a(km^{-1})$
tenuous	0.266	0.284	0.972
thick	0.292	1.431	1.531
thick plus	1.101	4.530	1.602
extra thick	1.912	7.648	1.684

The scattering phase function is a combination of Rayleigh and Mie scattering phase function with corresponding scattering coefficients, shown by (4)-(6) in [**?**]

$$P(\mu) = \frac{k_s^{Ray}}{k_s} p^{Ray}(\mu) + \frac{k_s^{Mie}}{k_s} p^{Mie}(\mu) \tag{2.1}$$

where $\mu = cos(\theta_s)$ is defined from the scattering angle θ_s. The two phase function follows a generalized Rayleigh and a generalized Henyey-Greenstein function, respectively, which is given by

$$p^{Ray}(\mu) = \frac{3[1 + 3\gamma + (1-\gamma)\mu^2]}{16\pi(1+2\gamma)} \tag{2.2}$$

$$p^{Mie}(\mu) = \frac{1-g^2}{4\pi}[\frac{1}{(1+g^2-2g\mu)^{3/2}} + f\frac{0.5(3\mu^2)-1}{(1+g^2)^{3/2}}] \tag{2.3}$$

In our simulation, we assume $\gamma = 0.017$, $g = 0.72$, $f = 0.5$ as our model parameter. Next we will briefly introduce three path loss models and present the experiment results.

2.2.1 Approximate Single Scattering Path Loss Model

This model assumes that the intersection cones are small, namely the apex angle is not too large. For a small overlap volume, V can be well approximated by a frustum of the right cone of volume $V = \frac{1}{3}\pi(D_1^2 h_1 - D_2^2 h_2)$, where $h_1 = r_1 + r_2\frac{\phi_2}{2}$ and $D_1 = h_1\frac{\phi_1}{2}$ are the height and the radius of the bottom surface of the large cone, and $h_1 = r_1 - r_2\frac{\phi_2}{2}$ and $D_2 = h_2\frac{\phi_1}{2}$ for the smaller cone. Therefore, we obtain the following path loss expression[22]

$$L \approx \frac{96 r sin\theta_1 sin^2\theta_2 (1 - cos\frac{\phi_1}{2}) exp[\frac{k_e r(sin\theta_1 + sin\theta_2)}{sin\theta_s}])}{k_s P(\mu) A_r \phi_1^2 \phi_2 sin\theta_s (12 sin^2\theta_2 + \phi_2^2 sin^2\theta_1)} \tag{2.4}$$

However, this model only provides high fidelity path loss approximation when the common volume is small, which limits its applicability for geometries with longer baseline distance or large volume overlap, such as large pointing angle or large FOV.

2.2.2 Empirical Path Loss Model

Through many field tests, author in [20] proposed a parametric path loss model as follows,

$$L = \xi r^{\alpha} \tag{2.5}$$

where ξ is the path loss factor and α is the path loss exponent. The estimated model parameters are present in Table 1 and 2 in[23]. For Rx pointing angle smaller than 20°, α is close to 2. In this case, path loss is very sensitive to distance. For Rx pointing angle larger than 70°, α is either close to 1 or less than 1, leading to low sensitive to distance. The small path loss exponent α corresponding to large Tx and Rx pointing angles does not mean that the total path loss is smaller for a larger pointing angle since it depends on the path loss factor ξ as well. In fact, ξ becomes dominant in overall path loss as angles increase. The

path loss factor changes by several orders of magnitude for varying Rx pointing angles at any given Tx pointing angle. The dynamic range under a small Tx pointing angle is larger than that under a large Tx pointing angle.

2.2.3 Monte Carlo Multiple Scattering Path Loss Model

We decomposed UV light into thousands of photons with individual photon's migration path and scattering probability. Using a large numbers of photons to simulate the progress of photon migration, we can roughly get a statistical path loss model.

After emission, each photon will follow a migration path along which it may be scattered or absorbed. The length of each migration between scattering event center is governed probabilistically, as is the renewed after each migration. The photon will keep migrate until it either reaches the receiver or its survival probability is smaller than threshold value.[**?**] After each interaction between a photon and a scattering center, the photon's propagation is assumed to follow the law of single scattering. Following this theory, the distance between two scattering interactions is given by the random variable,

$$\Delta_s = -\frac{ln\xi^{(s)}}{k_s} \tag{2.6}$$

where $\xi^{(s)}$ is a standard uniform random variable.

If a photon is scattered at angles (θ, ψ) offset from the incoming direction with

direction cosines $(\mu_x^i, \mu_y^i, \mu_z^i,)$, then the new direction cosines are calculated via

$$\begin{aligned}
\mu_x^{i+1} &= \frac{sin\theta}{\sqrt{1-(\mu_z^i)^2}}(\mu_x^i\mu_z^i cos\psi - \mu_y^i sin\psi) + \mu_x^i cos\theta, \\
\mu_y^{i+1} &= \frac{sin\theta}{\sqrt{1-(\mu_z^i)^2}}(\mu_y^i\mu_z^i cos\psi + \mu_x^i sin\psi) + \mu_y^i cos\theta, \\
\mu_z^{i+1} &= -sin\theta cos\psi\sqrt{1-(\mu_z^i)^2} + \mu_z^i cos\theta
\end{aligned} \tag{2.7}$$

Therefore, the new migration position is as follow:

$$(x_{i+1}, y_{i+1}, z_{i+1}) = (x_i, y_i, z_i) + (\mu_x^i, \mu_y^i, \mu_z^i)\Delta s \tag{2.8}$$

Each photon is assigned a survival probability, which is reduced due to energy loss and is update according to

$$w_n = (1 - p_{1n})e^{-k_a|r_n - r_{n-1}|}w_{n-1} \tag{2.9}$$

Here, p_{1n} is the probability that the receiver can see the photon within its FOV after photon scatters n times,

$$p_{1n} = \int_{\Omega_n} P(cos\theta)\delta\Omega \tag{2.10}$$

After n-th scattering interaction, the probability that the photon successfully arrives at receiver is given by

$$P_n = w_n p_{1n} p_{2n}, \qquad p_{2n} = e^{-k_e|r_n - r_{rx}|} \tag{2.11}$$

where, p_{2n} represents the propagation loss of the photon from the n-th scattering center to receiver.

An individual photon's spatial migration path can be uniquely described by five variables: thress spatial coordinates for the position and two direction angle θ and ψ. The photon's spatial position can be represented with three Cartesian coordinates and migration

direction can be described with three direction cosines from the two direction angles. The new migration direction is governed by the normalized phase function that describes the angular intensity of scattered light. The deviation from the current direction is determined from a standard uniform random variable $\xi^{(\mu)}$ and phase function eq. (2.1)

$$\xi^{(\mu)} = 2\pi \int_{-1}^{\mu_1} P(\mu) d\mu \tag{2.12}$$

Here, $\mu_1 = cos\theta$, where θ is the angle of the new photon path with respect to the current direction. The new migration position can thus be calculated via

Algorithm 1 MC method

$n = 1$

$N_t = 1e6$ (emitting photon number)

while $n \leq N_t$ **do**

    photon location $\Leftarrow Tx$

    scattering order $\Leftarrow 0$

    survival probability $\Leftarrow 1$

    while survival probability $\geq$ threshold **do**

        scattering order+=1

        Generate step size and move photon

        if With boundary **then**

            Calculate new direction

            Update propagation time

            Update survival and arrival probability

            if Survival probability $\leq$ threshold **then**

                Break

            end if

        else {out of boundary}

            break

        end if

    end while

    $n = n + 1$

end while

2.3 Experimental System Setup

It is clear that the validation of these models is an important research avenue, and prior work has demonstrated their accuracy at short range (less than 100 m) [24, 20]. Here, by reporting experimentally collected data, we illustrate two approaches to measuring path loss at longer ranges. In addition to highlighting practical issues that must be considered when performing such measurements, the data provide validation of a previously reported propagation model [25].

Fig. 2.2 illustrates the measurement system used to characterize UV NLOS path loss. The transmitter is a compact Q switched fourth-harmonic ND:YAG 266 nm laser that outputs 2.7 mJ pulses with a nominal pulse width of 3 ns. This provided sufficient energy for channel measurements out to several kilometers depending on the system geometry, which was adjustable through the use of rotation stages with precise motorized angular control. Synchronization between the transmitter and the receiver was achieved via an auxiliary optical-fiber channel. The received energy was detected through a solar-blind filter by one of the following two photomultiplier tube (PMT) systems that implemented either an analog or a digital measurement approach, and, in both cases, the resulting signal was recorded with an oscilloscope. The analog receiver system comprised a Hamamatsu H10304 PMT (with an integrated high-voltage circuit, an 8 mm active diameter, a gain of 2.3106, and a 6 ns response time) and a customized high-gain (34 dB) 1.5 GHz preamplifier. The voltage output of this receiver is, hence, modeled as being proportional to the number of incident photons with a fixed constant of proportionality. However, this model may fail for short-duration (and, to a lesser extent for practical experiments, high-amplitude) received signals,

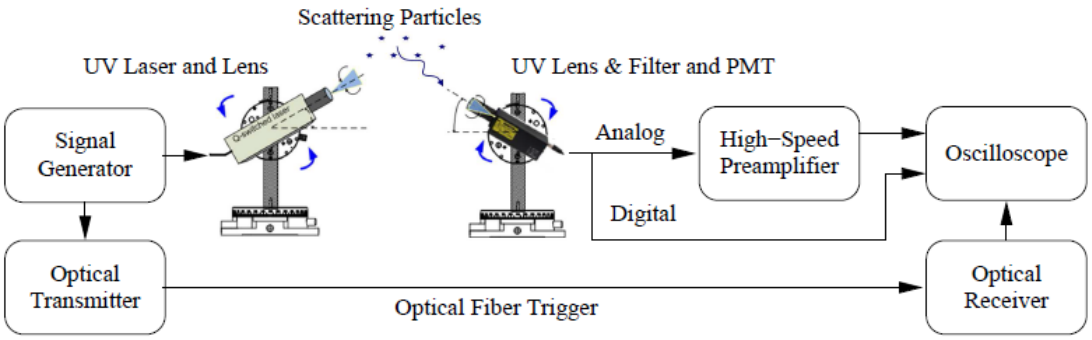

Figure 2.2: NLOS UV Channel measurement platform.

which may challenge both the linearity and the bandwidth of the system. Meanwhile, the digital receiver system used a PerkinElmer MP1922 photon-counting module that outputs a standard transistor-transistor-logic pulse when a photon is detected. In this case, however, the finite response time of the device can lead to saturation of the PMT for high-amplitude received signals. Hence, received-signal duration is more critical to the measurement fidelity of the analog system, whereas received-signal amplitude is more critical to the digital system, a distinction that can have practical consequences for the two approaches.

2.4 Initial Experimental Results

2.4.1 NLOS Long Distance Impulse Response Measurements

A series of measurements were conducted including varying the Tx and Rx elevation angles from 10 to 90 degree and the distance between Tx and Rx is 400 m and 758m. Fig. 2.3 and Fig. 2.4 show the impulse response at 400 m when the Tx angle is 20° Rx angel is 10° and 70°. The resulting FWHM pulse width varies from 200 ns to 400 ns. The

red opposite pulse is the receive signal out of analogy PMT. Light green represents the synchronize signal from optical fiber. And the green one is the signal out of digital PMT.

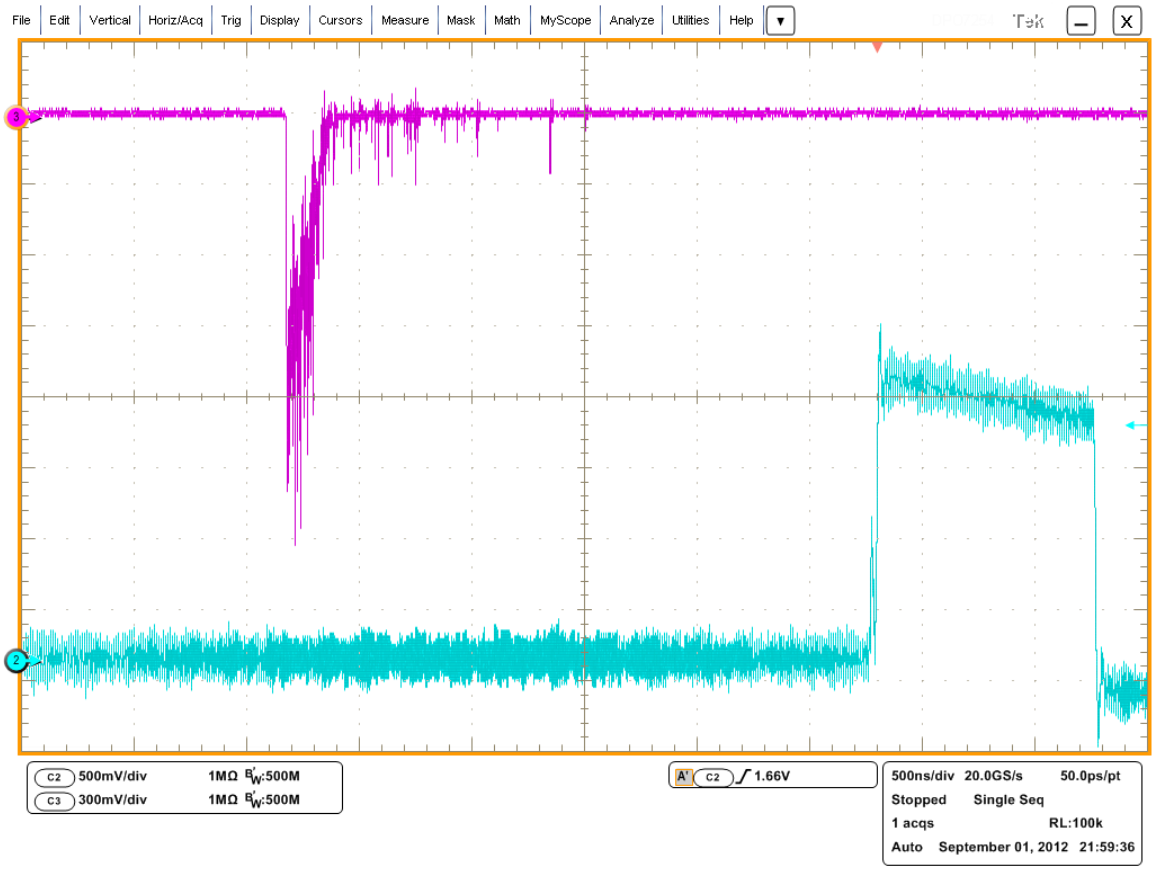

Figure 2.3: Impulse response. r=400 m , Tx=20°, Rx=10°.

Note the faster rising edge, followed by slower decay. The decay increases as the elevation angle increases, due to the larger spread in propagation times for scattered photons. With a smaller elevation angle (lower to the horizon), the decay becomes significantly sharper and the pulse width is decreased.

Fig. 2.5 and Fig. 2.6 show the impulse response at 400 m when the Tx angel is

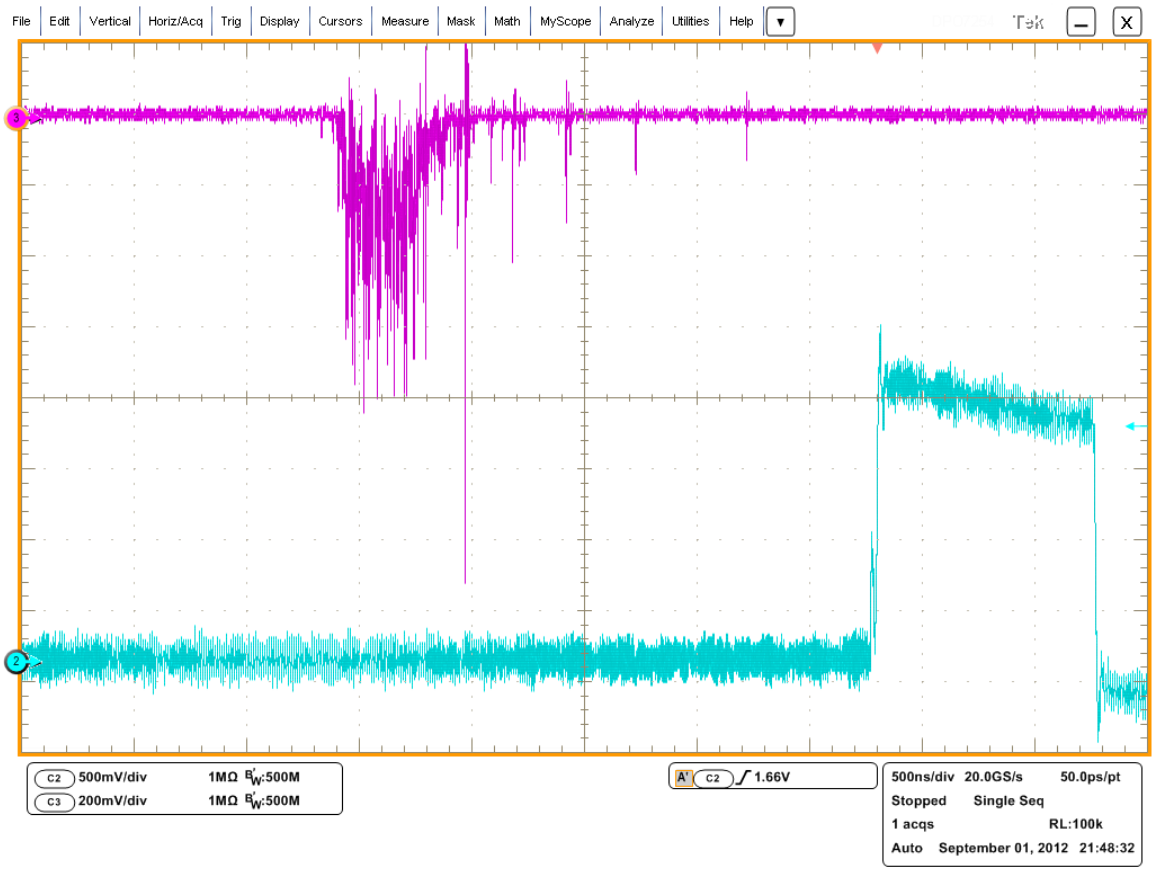

Figure 2.4: Impulse response. r=400 m, Tx=20°, Rx=70°.

5°0 Rx angel is 10° and 70°. The resulting FWHM pulse width varies from 500 ns to 1 us.

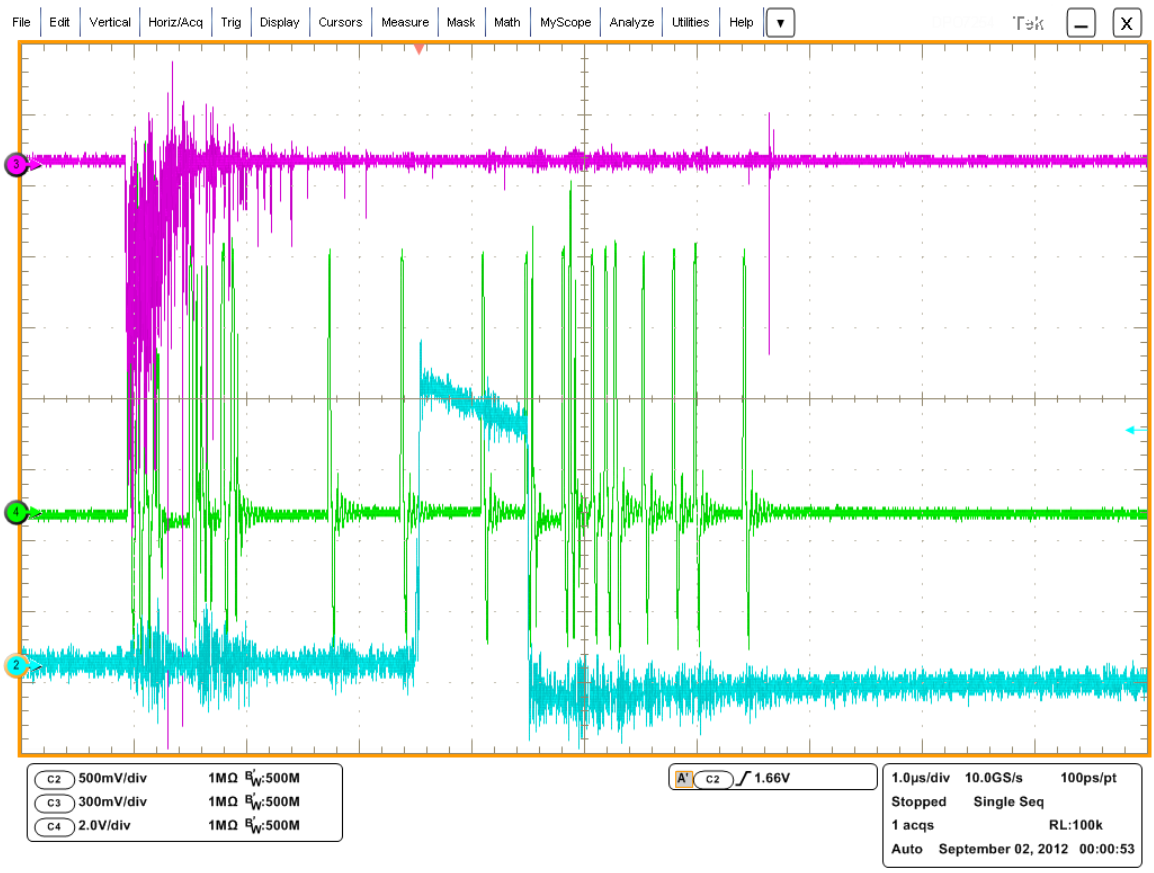

Figure 2.5: Impulse response. r=400 m , Tx=50°, Rx=10°.

From the latter two figures, sometime we also can get some digital signal after most photon arrived. There are two reasons: one is the threshold is not optimized, the digital PMT converts noise to normal pulse; the other reason is that part of photon actually arrived the front end due to large time multi scattering. However, we still can tell from the number of pulse to judge whether the transmitter send 1 or 0 in one slot (we implement based on USRP). Because the higher the angle, the longer the path a photon need to surfer before

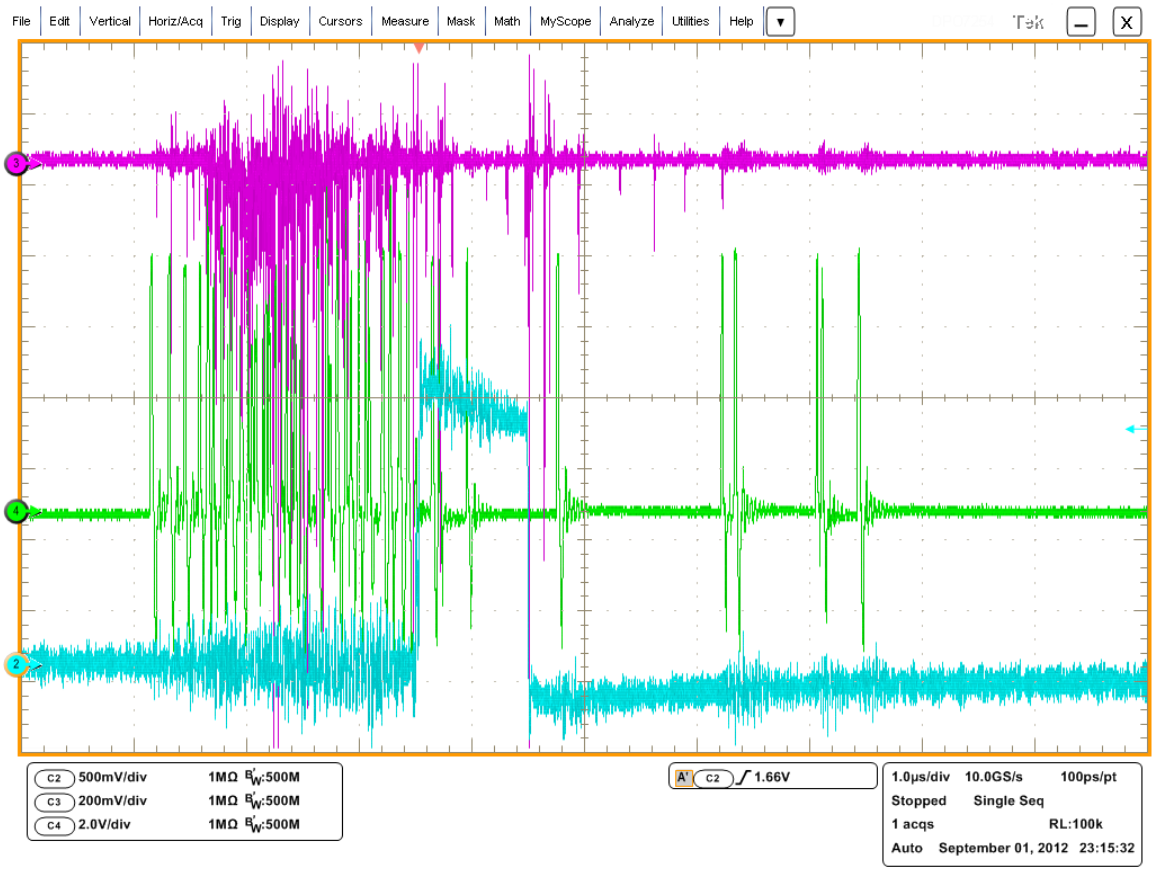

Figure 2.6: Impulse response. r=400 m, Tx=50°, Rx=70°.

arriving the receiver. Therefore the FWHM will vary on different geometry configuration causing different achievable date rate. We can find that the high pointing angel make the signal close to the synchronized signal (assume fixed). This also approve that the higher angel, the longer the path photons need to suffer before arriving. Note that the spikes increase as the elevation angel increases, due to the long range atmosphere is more complex than short range, where only signal scattering and negligible turbulence.

2.4.2 NLOS Long Distance Path Loss Measurements

The path loss L is defined as the average ratio of transmitted and received power per pulse, where the latter is obtained from average received photon counts. We employed a high-performance power meter to measure E_{Tx}, the transmitted optical energy per pulse in Joules. (A photon counting system would be easily saturated if used for such a direct measurement.) The energy per photon is given by hc/λ, where h is Planck's constant, c is the speed of light, and λ is the photon wavelength. Therefore, the number of transmitted photons per pulse N_{t} can be computed as

$$N_{\mathrm{t}} = E_{\mathrm{Tx}}\lambda/(hc). \tag{2.13}$$

We denote the number of detected photons per pulse by N_{d}, which is a fraction (due to losses from optical filtering, detector quantum efficiency, etc.) of the number of arriving photons, N_{r}. In particular, N_{d} can be expressed as

$$N_{\mathrm{d}} = N_{\mathrm{r}}\eta_{\mathrm{f}}\eta_{\mathrm{q}}, \tag{2.14}$$

where η_{f} is the filter transmittance and η_{q} is the PMT detection efficiency. The path loss

in decibels is therefore defined by

$$L = 10\log_{10}\left(\frac{E_{\mathrm{Tx}}\lambda\eta_{\mathrm{f}}\eta_{\mathrm{q}}}{hcN_{\mathrm{d}}}\right). \tag{2.15}$$

It should be noted that E_{Tx} varied with temperature. As such, a measurement of E_{Tx} was taken for each tested system geometry, and E_{Tx} was found to be in the range of 2.1 mJ to 4.3 mJ. The overall filter transmittance η_{f} varied depending on which optical attenuation filter was employed in addition to the solar-blind filter, which had a filter attenuation of 0.13. (As previously discussed, the additional attenuation was used to to avoid light levels that would result in detector saturation.) Finally, the PMT quantum efficiency η_{q} was 0.10.

In our experiment, we employed high speed photon counter to calculation the receive number of photons. Fig. 2.7 and 2.8 show the path loss with different geometry corresponding to distance 400m and 758m.

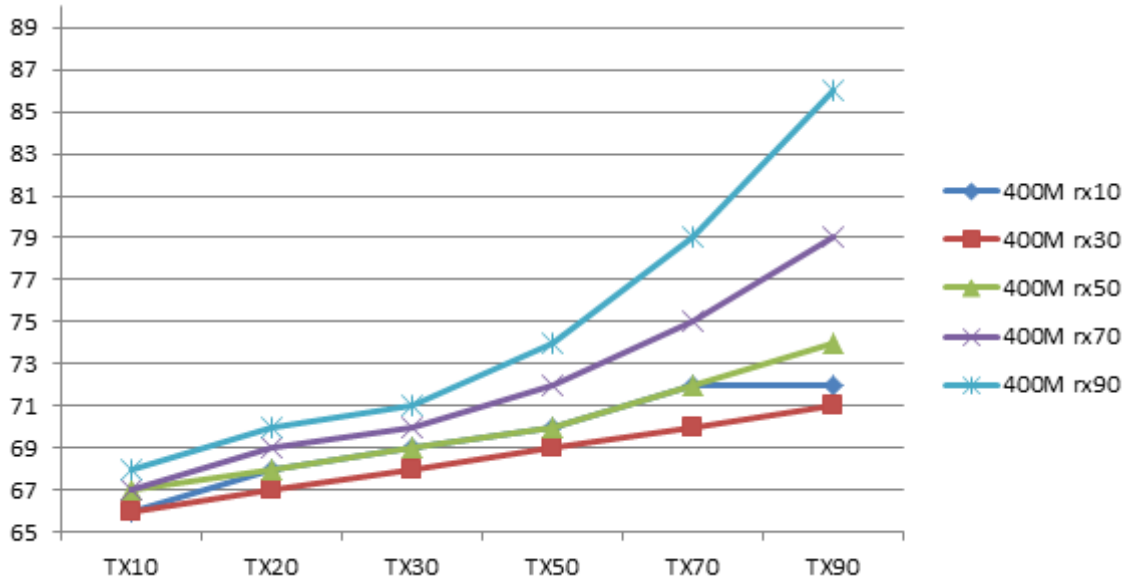

Figure 2.7: Path loss with different geometry. r=400 m.

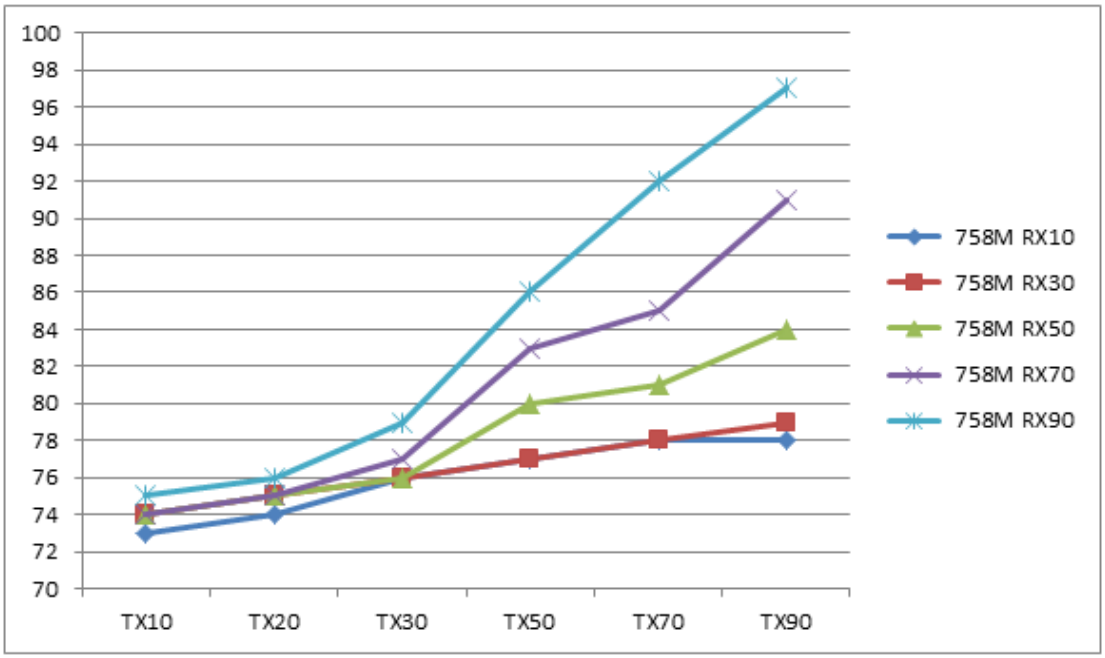

Figure 2.8: Path loss with different geometry. r=758 m.

From Fig. 2.9 we note that as the elevation angel increase, the path loss become increase faster than the lower point angel. And the longer distance, the larger path loss with same geometry configuration.

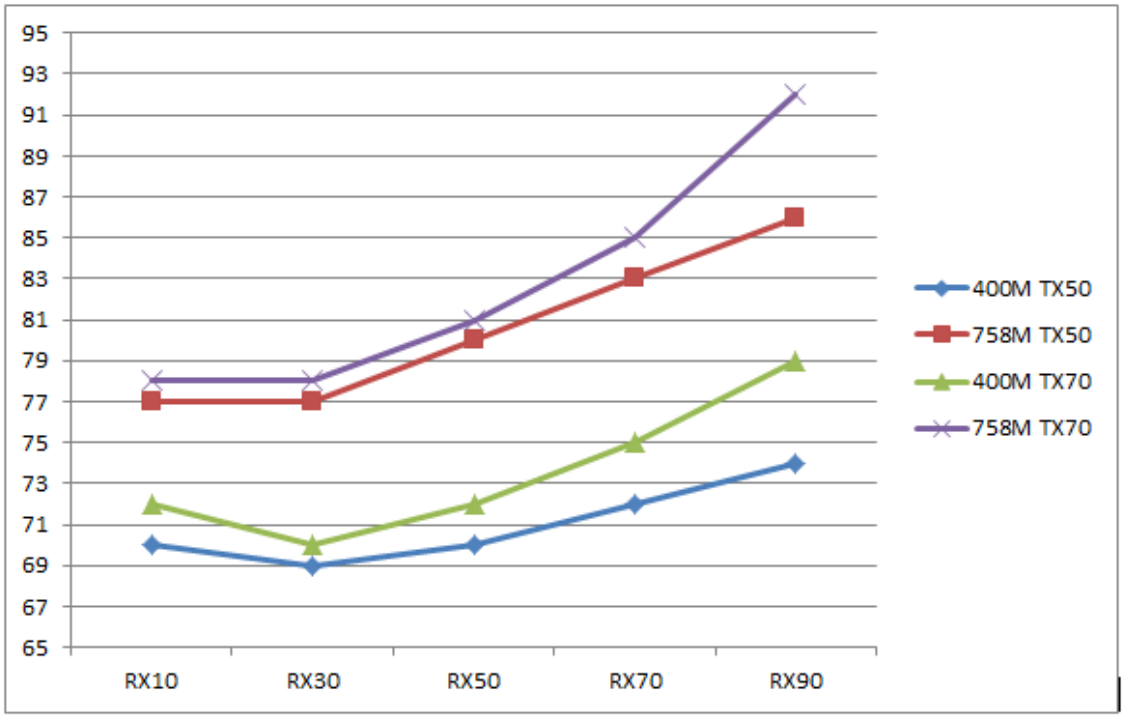

Figure 2.9: Comparison between different distances.

2.4.3 Measurement Results Compare with Simulation Results

Haipeng already used Monte Carlo (MC) [7] to predict the path loss in long range. Based on his code, army research center compared the measurement results with the simulation results as Fig. 2.10 and Fig. 2.11.

The estimates based on the analog PMT agree well with predictions at 758 m,

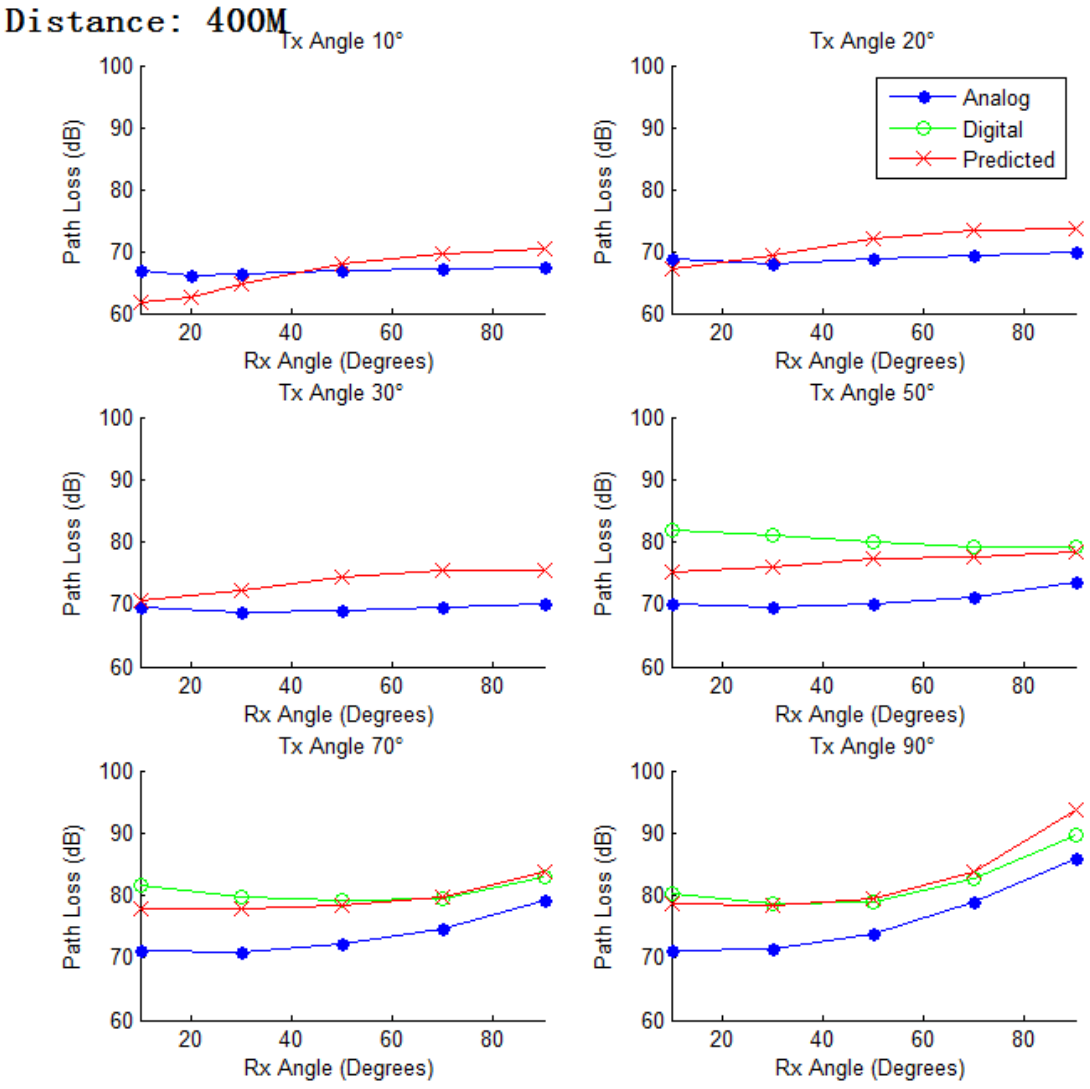

Figure 2.10: Comparison between different distances.

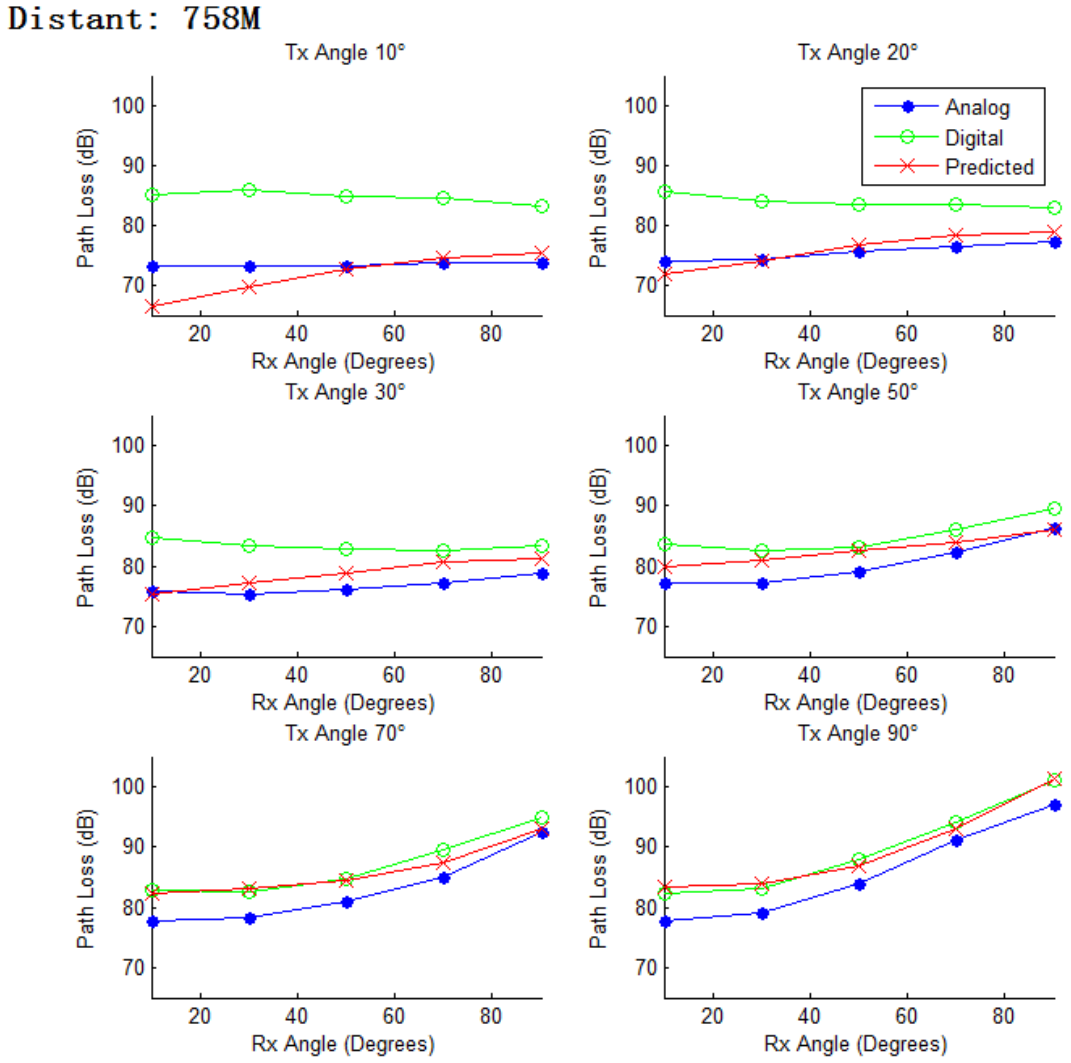

Figure 2.11: Comparison between different distances.

but deviate from both the digital PMT estimates and the theoretical model at 400 m. We believe this discrepancy is in part attributable to measurement distortion arising from the decreasing width of the received signal pulse as range and elevation angles are decreased. Similarly, the digital PMT results agree well with model predictions except at very low elevation angles, where the device has clearly saturated. In fact, the digital PMT estimates at 400 m increase as the receiver elevation angle decreases, a perhaps counterintuitive result. However, this is explained by noting that the received-pulse width is also decreasing, implying that the saturated digital receiver is detecting photons over a decreasing period of time and, hence, yielding a lower received-energy estimate. The analog and digital estimation errors may be mitigated through the use of longer transmitted pulses with lower amplitude or by adding supplemental optical attenuation at the receiver, though the former option may be limited by the desire to test at long ranges. In any case, the experimental results validate well the theoretical model within the practical limitations previously discussed.

2.5 Summary

Some basic concepts of NLOS UV channel characteristics and basic channel path loss models are introduced. What's more, we compare an analog and a digital method for characterizing the long-distance non-line-of-sight ultraviolet scattering channel. Initial experimental results and theoretical-model predictions are presented that provide demonstration and validation. According to those discrepancies and issues, we design another outdoor experiment in next chapter, which is much more comprehensive.

Chapter 3

Long Distance Non-Line-of-Sight Ultraviolet Communication Channel Analysis Based on UV Laser

3.1 Introduction

In this chapter, we detail a long-distance NLOS UV channel sounding experiment in which path loss, pulse broadening, and scintillation effects were measured at distances up to 4 km. To the best of our knowledge, this experiment represents the most comprehensive examination of the NLOS UV communication channel at such distances. The experimental results are compared with predictions from a Monte Carlo multiple-scattering channel

model, providing reasonable validation of this model at long distance. In addition, we examine the distribution of received photon counts for evidence of the effects of turbulence in the NLOS channel. In this case, however, there is less agreement with predictions from existing turbulence models, suggesting the need for additional research on the refinement of turbulence modeling. Finally, we discuss implications of the measurement and modeling results for long-range communication performance.

3.2 UV Communication Test Bed, Experimental Conditions and Basic Methodology

The data collection experiment was conducted in an open field near Joshua Tree Desert, Twentynine Palms, CA, during the night hours of 9 p.m. to 5 a.m. from June 6 to June 9, 2013. Noise measurements indicated that background noise was negligible with respect to the data collected, and the atmospheric conditions (e.g., the atmospheric constituents) appeared consistent throughout the experiment. The outdoor temperatures ranged from 23.8 °C to 33.8 °C, the average wind speed during the testing period was 3.86 m/s, and the average relative humidity was 16.14%. All of the reported data were collected using the UV laser measurement system depicted in Fig. 3.1.

The transmitter was a compact Q-switched fourth-harmonic ND:YAG 266 nm laser that transmitted pulses with an average optical output power of 3.3 mJ (sufficient for channel measurements up to several kilometers) with a nominal pulse width of 3 ns and a 3 mrad full-angle beam width. The pointing directions of the transmitter and receiver were

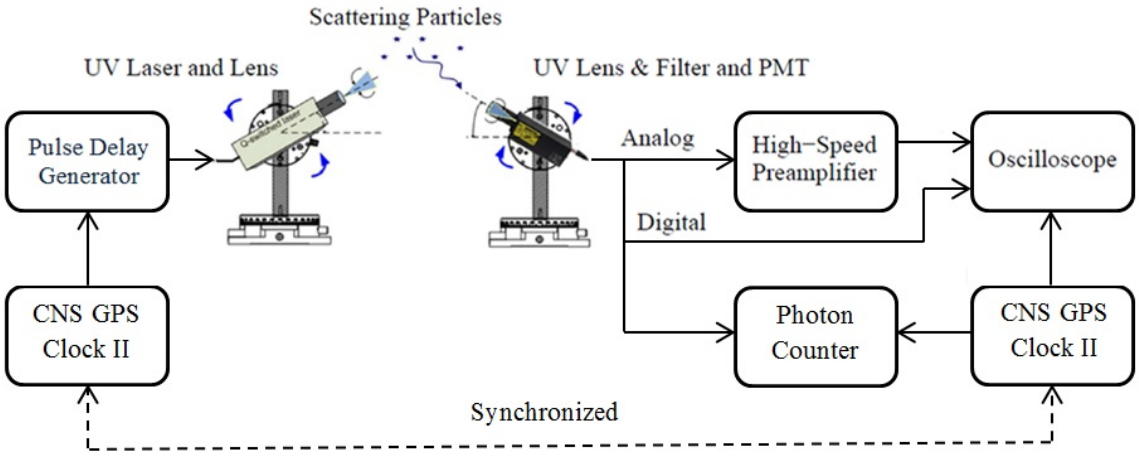

Figure 3.1: NLOS UV channel measurement system.

adjusted through the use of rotation stages with precise motorized angular control. Synchronization between the transmitter and the receiver was achieved with two synchronized GPS CNS II clocks that output one pulse per second timing signals. At the transmitter, the GPS signal was fed into a pulse delay generator, the output of which served as a laser trigger.

The received energy was detected after solar-blind filtering by two photomultiplier tube (PMT) systems, one using an analog measurement approach and the other using a digital approach. The analog receiver system comprised a Hamamatsu H10304 PMT (with an integrated high-voltage circuit, 8 mm active diameter, gain of 2.3×10^6, and 6 ns response time) and a customized high-gain (34 dB) 1.5 GHz preamplifier. The voltage output of this receiver is modeled as being proportional to the number of incident photons with a fixed constant of proportionality. We note that this model may fail for short-duration high-intensity receive signals, which can challenge both the linearity and the bandwidth of the

system.

The digital receiver system employed a PerkinElmer MP1922 photon-counting module that sent a standard transistor-transistor-logic pulse when a photon was detected. It was responsive to wavelengths from 165 nm to 320 nm with 10 dark counts per second. The peak quantum efficiency of 15% and the peak gain of 10^6 occurred at a wavelength of 200 nm, and the quantum efficiency decreased to 10% at 260 nm and 7% at 280 nm. For this system, the finite response time (or dead time) of the photon-counting system can lead to saturation for high-intensity received-signals, due to photons arriving while the system is in a reset state following a previously detected photon [26],[27].

While receiver saturation could be a potential issue with both systems, it seems that received-signal duration may be more critical to the measurement fidelity of the analog system, whereas received-signal amplitude may be more critical to the digital system, a distinction that could have practical consequences for the two approaches. In any case, to mitigate the potential adverse effects of saturation, one optical filter from a set of filters, each with a different attenuation (5.5 dB, 21.54 dB, 33.4 dB, and 44.6 dB), was mounted on the solar blind filter to reduce the received-signal strength in a controlled manner. The specific filter used for each measurement depended on the particular link geometry under investigation; our selection was based on predictions from a Monte Carlo channel model computed prior to the experiment.

Both the analog and digital PMTs had a circular sensing window with a diameter of 1.5 cm, resulting in an active area of 1.77 cm^2. Based on measurements, the effective field of view (FOV) for each detector (combining the PMT, solar blind filter, and attenuation

filters) was estimated to be 30°.

The signals output by each receiver system were recorded using an oscilloscope triggered by the receiver-side GPS system with an appropriate propagation time delay. In addition to the oscilloscope data, photon counts for each pulse were recorded using an SR400 two-channel gated high-speed photon counter with a 200 MHz sample rate and a 200 mV threshold, also triggered by the GPS clock. The two counting channels were used to record the photon detections in two back-to-back 30 ms intervals, with the first interval synchronized with the received pulse. Because the received pulse was shorter than 30 ms for all considered system geometries, the second counting channel provided a statistical measurement of the background noise; as a result of those noise measurements, we concluded that the count rate of the background noise was effectively zero counts per received pulse.

Figure 3.2 shows an oscilloscope screenshot when system geometry was set to $(\theta_1, \theta_2, r) = (70°, 30°, 1000 \text{ m})$. The pink curve represents the (inverted) response from the analog PMT, the light green curve is the 1 pulse per second signal from the synchronized GPS, and the dark green curve is the output from the digital PMT. From this screenshot, we see that the precise timing of the GPS signal provides a highly effective method to achieve synchronization for data capture.

3.3 The Verification of Prior Channel Model

Measurements were taken for a variety of system geometries. In particular, the transmitter and receiver were positioned at various distances pointed at each other (i.e., in a coplanar geometry) with varying elevation angles. For each system geometry, received

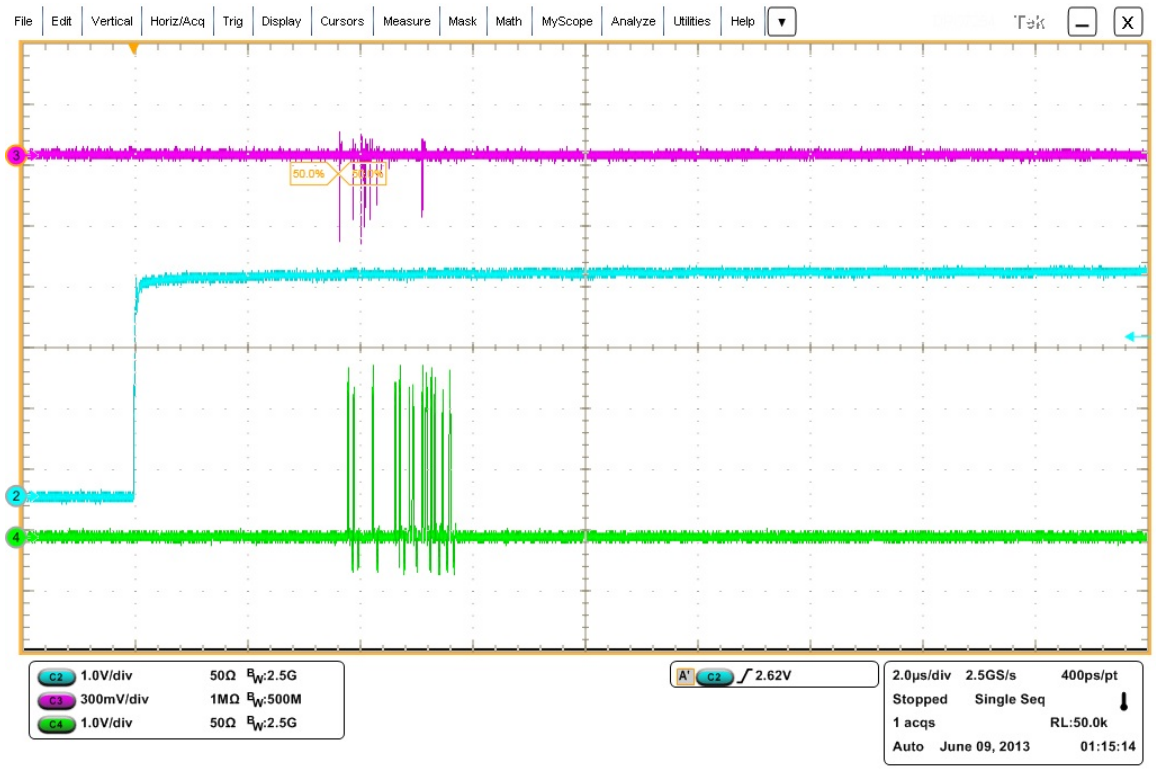

Figure 3.2: Screenshot of an oscilloscope display.

photon counts for 200 independent transmitted pulses were recorded by the digital PMT, and analog current waveforms (approximating the impulse response of the system) for 50 independent transmitted pulses were recorded by the analog PMT. From this data set, the average received photon count (which can be converted to the average received energy) and the average pulse broadening could be calculated as a function of the system geometry parameters (i.e., the separation distance and pointing angles).

3.3.1 NLOS UV Path Loss

We adopted the channel model in [7] to compute theoretical path loss predictions that were used to compare to experimentally estimated values. Consistent with

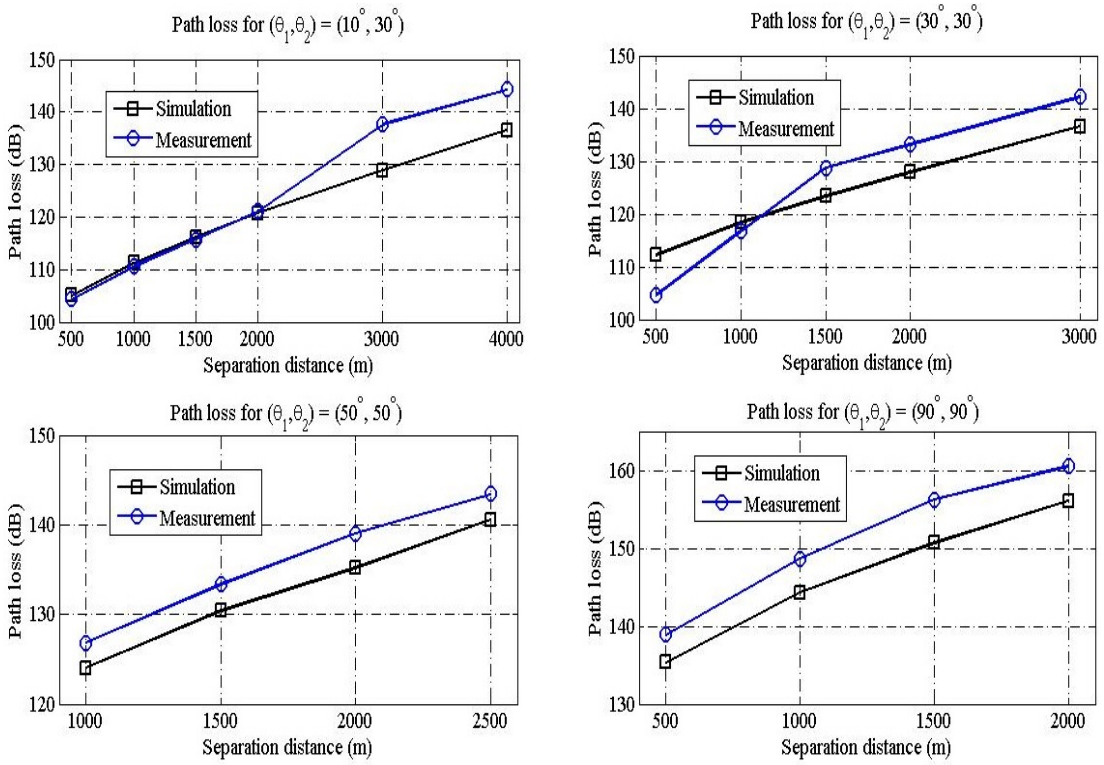

Figure 3.3: Comparison of model predictions and experimental estimates of path loss for four system configurations.

experimental conditions, the Monte Carlo simulation parameters were set as following: $(\phi_1, \phi_2, \gamma, f, g, k_{\rm a}, k_{\rm s}^{\rm Ray}, k_{\rm s}^{\rm Mie}) = (3$ mrad, 30°, 0.017, 0.72, 0.5, 0.972 km^{-1}, 0.266 km^{-1}, 0.284 km^{-1}), where γ, f, and g are phase function parameters [22, 28] and $k_{\rm a}$, $k_{\rm s}^{\rm Ray}$, and $k_{\rm s}^{\rm Mie}$ are the absorption coefficient, Rayleigh scattering coefficient, and Mie scattering coefficient, respectively.

Typical field test results and corresponding theoretical path loss estimates are shown in Fig. 3.3, where the path loss was normalized to a 1.77 cm^2 detection area and attenuation due to system devices (e.g., filters and PMT efficiency) was taken into account. The high path loss associated with long-distance NLOS UV communication is apparent,

with most of the reported path loss estimates exceeding 120 dB and in one case reaching 160 dB. The high sensitivity of the path loss estimates to the pointing angles is also noteworthy. In particular, path loss substantially increased as the pointing elevation angles increased, quantifying the additional transmit power necessary to maintain a given level of communication performance as a function of the elevation angles.

A reasonable agreement between theoretical channel model predictions and the measured data is observed, especially when the pointing angles of the transmitter and receiver elevation were low. Nevertheless, a mismatch of 3–10 dB did occur. While much of this error was likely attributed to tolerances in the estimation of the system and channel parameters, it is certainly a point of interest to isolate the sources of error. For example, one possible factor was the presence of turbulence, which has been hypothesized to affect the characteristics of the received-signal in NLOS UV communications. We further investigate the possible effects of turbulence in Section 4.

3.3.2 Pulse Broadening Effect

The examination of the broadening of pulses as they propagate through the NLOS UV scattering channel can provide insight into the bandwidth and achievable data rate of NLOS UV communication systems. Utilizing the digital and analog receiver systems, we characterized pulse broadening as a function of the transmitter elevation angle, the receiver elevation angle, and the separation distance, again focusing on distances that have not been sufficiently studied.

As in [29], we adopt the full width at half maximum (FWHM) of the received signal as a potentially useful metric for quantifying the pulse broadening of UV signals.

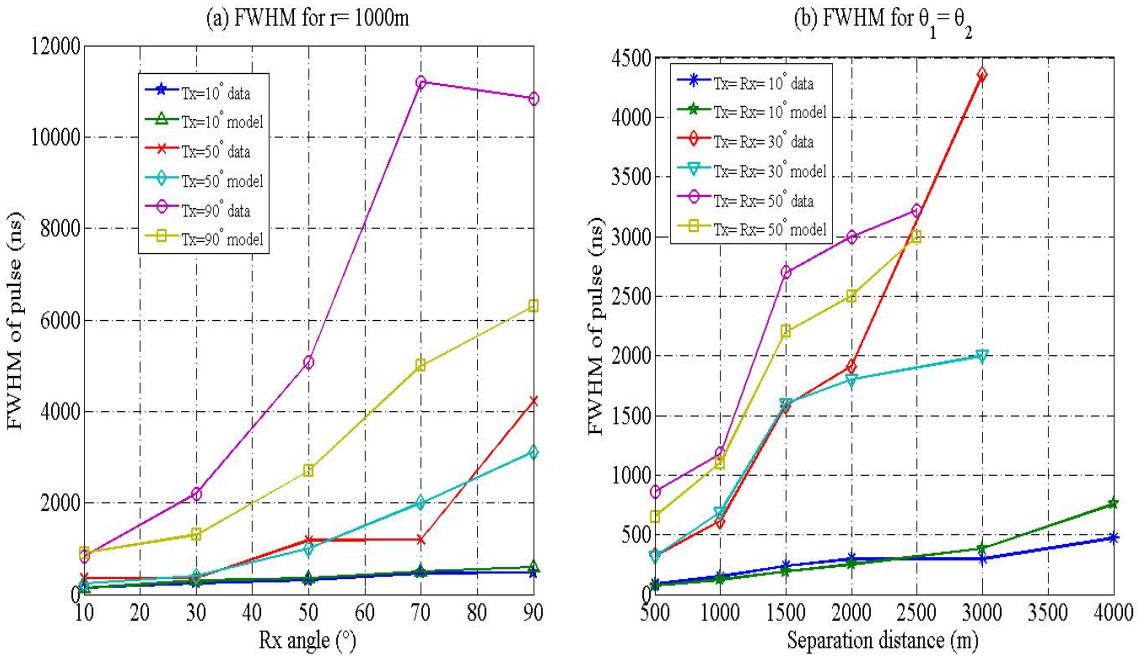

Figure 3.4: Comparison of model predictions and experimental estimates of the FWHM of received pulses for several system geometries.

It should be noted that each measured impulse response exhibited random variations due to the probabilistic nature of the received signal. This can be especially problematic for configurations where the detected signal is weak. As such, we averaged over 50 realizations of the impulse response per geometry in order to obtain an average response for each configuration. Then we calculated the FWHM for each geometry using this average impulse response, generally for both PMT systems. However, when the received-signal strength was extremely weak, only the data from the digital PMT was used, as the output gain of analog PMT was not sufficient to obtain reliable measurements.

Figure 3.4(a) compares model predictions and experimental estimates of the FWHM pulse widths as a function of elevation angles at a distance of 1 km. For low transmitter

pointing angles, the pulse-width estimates increase relatively slowly, whereas the rate of broadening grows significantly faster for higher transmitter pointing angles. Figure 3.4(b) depicts the relationship between the FWHM pulse widths and the baseline distance for three pairs (θ_1, θ_2) of transmitter and receiver elevation angles: (10°, 10°), (30°, 30°), (50°, 50°). Rapidly increasing pulse widths are observed as the distance increases for higher point angles. For example, FWHM pulse widths are in the range of 323 ns to 4.36 μs when pointing angles are set to 30°. The rate at which pulse widths increase with range is significantly less for lower pointing angles. For example, the experimental estimates of the pulse widths range from 85.6 ns to 470 ns for pointing angles of 10°.

Finally, we note that Fig. 3.4 shows reasonable qualitative agreement between the model predictions and experimental estimates of the pulse widths for low pointing angles, and we speculate that the mismatch for high pointing angles is due in part to inaccurate atmospheric parameters for the channel model, calibration errors, and other measurement errors. In any case, these measurement and modeling results provide rough guidelines regarding the system configurations for which intersymbol interference may become a significant factor in the design of a NLOS UV communication system.

3.4 The Infer of NLOS UV Scintillation Phenomenon

3.4.1 Path Loss Attenuation

In the literature, line-of-sight (LOS) UV turbulence models [30, 31] have been adapted to the NLOS case by noting that the single-scattering NLOS geometry consists of two LOS paths: the transmitter to the common volume V and the common volume V to the

receiver. Here, we review this modeling approach and examine experimental measurements for evidence of its validity.

Applying the Rytov approximation [32, 33], the scintillation attenuation of the two LOS paths are given by

$$\alpha_{r_1} = 2\sqrt{23.17 C_n^2 (2\pi/\lambda)^{7/6} r_1^{11/6}}, \tag{3.1}$$

and

$$\alpha_{r_2} = 2\sqrt{23.17 C_n^2 (2\pi/\lambda)^{7/6} r_2^{11/6}}, \tag{3.2}$$

where C_n^2 is the index of refraction structure parameter, which is altitude dependent and typically varies from 10^{-13} m$^{-2/3}$ for strong turbulence to 10^{-17} m$^{-2/3}$ for weak turbulence. The overall NLOS scintillation attenuation can then be approximated as the sum of the two independent path effects:

$$\alpha_{\text{turb}} \approx \alpha_{r_1} + \alpha_{r_2}. \tag{3.3}$$

The strength of scintillation is characterized by the scintillation index, expressed as

$$\sigma_{\text{I}}^2 = e^{\sigma_1^2} - 1, \tag{3.4}$$

where σ_1^2 is the log-intensity variance defined by

$$\sigma_1^2 = 1.23 C_n^2 k^{7/6} d^{11/6} \tag{3.5}$$

for a plane wave, with k denoting the vector wave number $(2\pi/\lambda)$ and d denoting the channel length. According to the scintillation index, turbulence strength can be roughly divided into four regions: negligible-weak, weak-moderate, moderate-strong, and strong, corresponding to scintillation indexes of 0–0.2, 0.2–1.6, 1.6–3.5, and over 3.5, respectively.

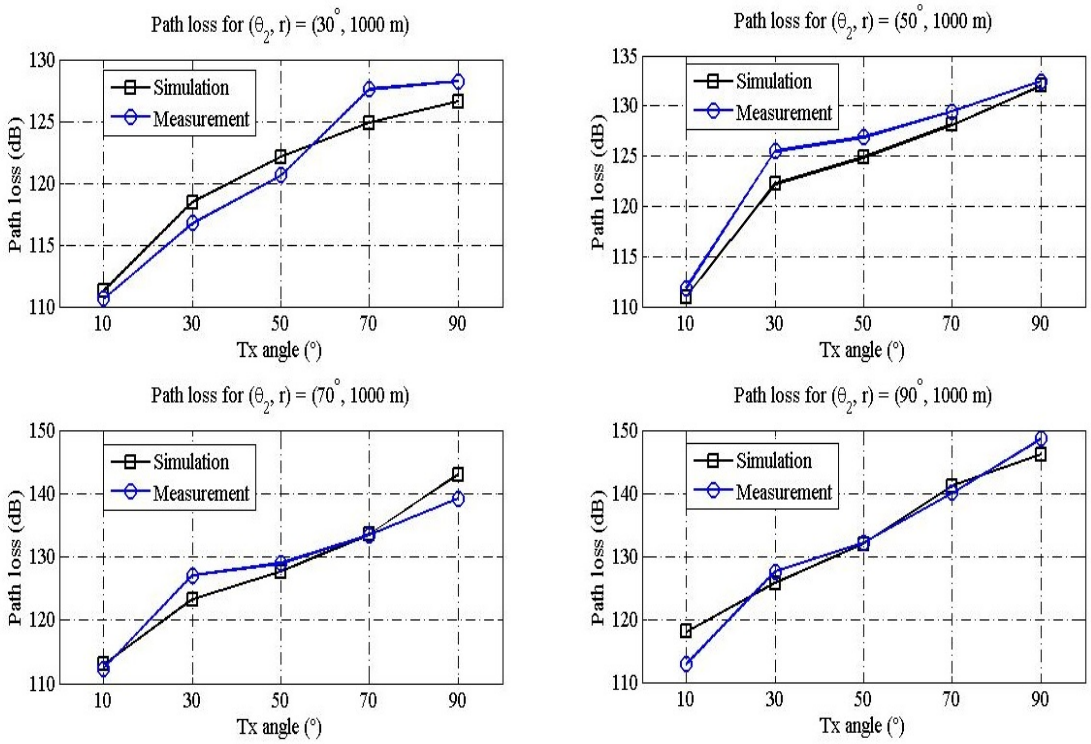

Figure 3.5: Comparison of turbulence-model predictions and experimental estimates of path loss for several system geometries.

If the turbulence is estimated to be greater than weak, then scintillation attenuation may have a significant effect on path loss.

Consistent with reported weather conditions, we assume that the experiment was conducted under weak-medium turbulence conditions. Therefore, we set C_n^2 to 10^{-16} $\mathrm{m}^{-2/3}$ in the turbulence model to illustrate the predicted effects of turbulence of such magnitude and to determine if those effects represent a plausible explanation for characteristics of the observed data. Figure 3.5 compares measured path loss estimates with model predictions obtained by applying the theoretical turbulence attenuation to the Monte Carlo path loss channel model estimates. Incorporating the turbulence attenuation model has reduced

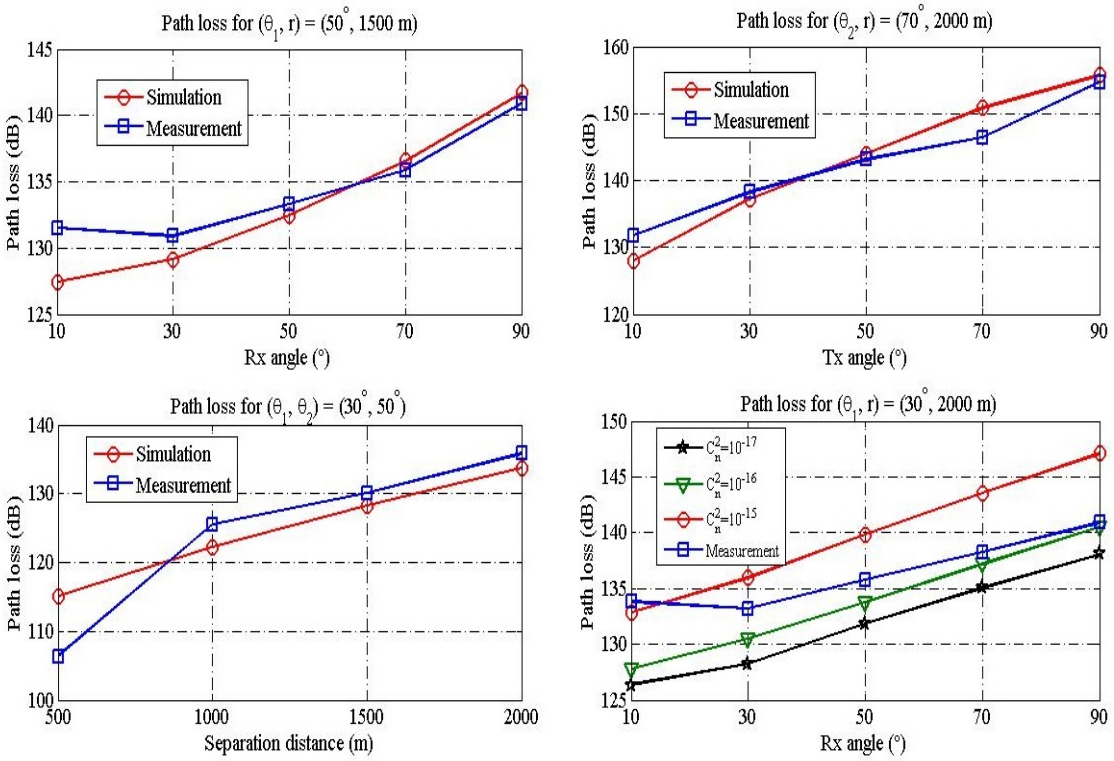

Figure 3.6: Comparison of turbulence-model predictions and experimental estimates of path loss for several scenarios.

the error between the measured and predicted path losses, supporting the significance of turbulence attenuation in the NLOS UV channel. Nevertheless, additional controlled experimentation and theoretical modeling are necessary to truly confirm this, since there are several potential sources of error that could explain the (uncompensated) estimation error.

Figure 3.6 further investigates the path loss predictions of the turbulence model for several long-distance scenarios. Figure 3.6(a) shows the model predictions and measurements of path loss against receiver pointing angle for fixed transmitter pointing angle and range, Fig. 3.6(b) presents the comparison between simulated data and field test results of path loss against transmitter pointing angle for fixed receiver pointing angle and range, and

Fig. 3.6(c) describes the measurements and model predictions of path loss versus separation distance for a particular pair of transmitter and receiver pointing angles. Agreement between theoretical and experimental estimates is observed in each of the three figures.

Finally, we examine how the assumed magnitude of turbulence affects the model predictions of path loss by considering various choices of C_n^2. The resulting model predictions are presented in Fig. 3.6(d), along with the field test results for comparison. The predicted path losses varies by about 10 dB depending on the choice of C_n^2. When the receiver pointing angle is low, the experimental measurements are most consistent with the model prediction corresponding to $C_n^2 = 10^{-15}$. However, when the receiver pointing angle is high, the experimental measurements are most consistent with the model predictions corresponding to $C_n^2 = 10^{-16}$. As this dependence on elevation angle is not clear from the theoretical modeling framework, additional study is warranted.

3.4.2 Irradiance Fluctuations

Besides causing additional signal attenuation, optical turbulence effects may also cause irradiance fluctuations. However, turbulence effects are often ignored in UV NLOS channel models, which typically focus on relatively short distances where the turbulence effects are expected to be negligible. In fact, irradiance fluctuations may degrade communication performance as the distance increases, where irradiance fading may significantly affect the received signal distribution. According to the Rytov solution to the wave equation, the log-amplitude variance is proportional to $\lambda^{-7/6}$. Therefore, the irradiance fluctuations due to atmospheric turbulence might be two or three times greater in the UV band compared to the visible band; hence, it is possible that UV links may be more sensitive to turbulence

than visible-light links. In this section, the PDFs of received photon counts are studied experimentally and with theoretical modeling to characterize possible turbulence-induced irradiance fluctuations.

For weak and moderate turbulence, it has been observed that the PDF of the LOS received intensity is well modeled by a log-normal (LN) distribution. With the irradiance denoted by I, the log-normal distribution is given by the following:

$$p(I) = \frac{1}{I\sqrt{2\pi\sigma_{\mathrm{l}}^2}} \exp\left\{-\frac{[\ln(I/I_0) + \sigma_{\mathrm{l}}^2/2]^2}{2\sigma_{\mathrm{l}}^2}\right\} \tag{3.6}$$

where I_0 is the mean received irradiance and σ_{l}^2 is defined in (3.5).

Once again, we apply the approximation of the NLOS path as consisting of two segments: the transmitter to common volume and common volume to the receiver [17]. As such, the irradiance at the common volume has a LN PDF $f_X(x)$, and the conditional arrival power level at the receiver has a LN PDF $f_{Y|X}(y|x)$, where X and Y represent the power levels at the common volume and the receiver, respectively. Lastly, σ_x^2 and σ_y^2 can be calculated from (3.5). The joint PDF for X and Y is therefore

$$f_{X,Y}(x, y) = f_{Y|X}(y|x) f_X(x), \tag{3.7}$$

and the PDF of the received power Y is

$$f_Y(y) = \int f_{X,Y}(x, y) dx. \tag{3.8}$$

Figure 3.7 illustrates the estimated received-count PDFs based on the theoretical model and the experimental measurements. We note significant mismatch between the theoretical turbulence-based and measured PDFs, though the general features and characteristics are captured by the model. It is also well known that shot noise contributes

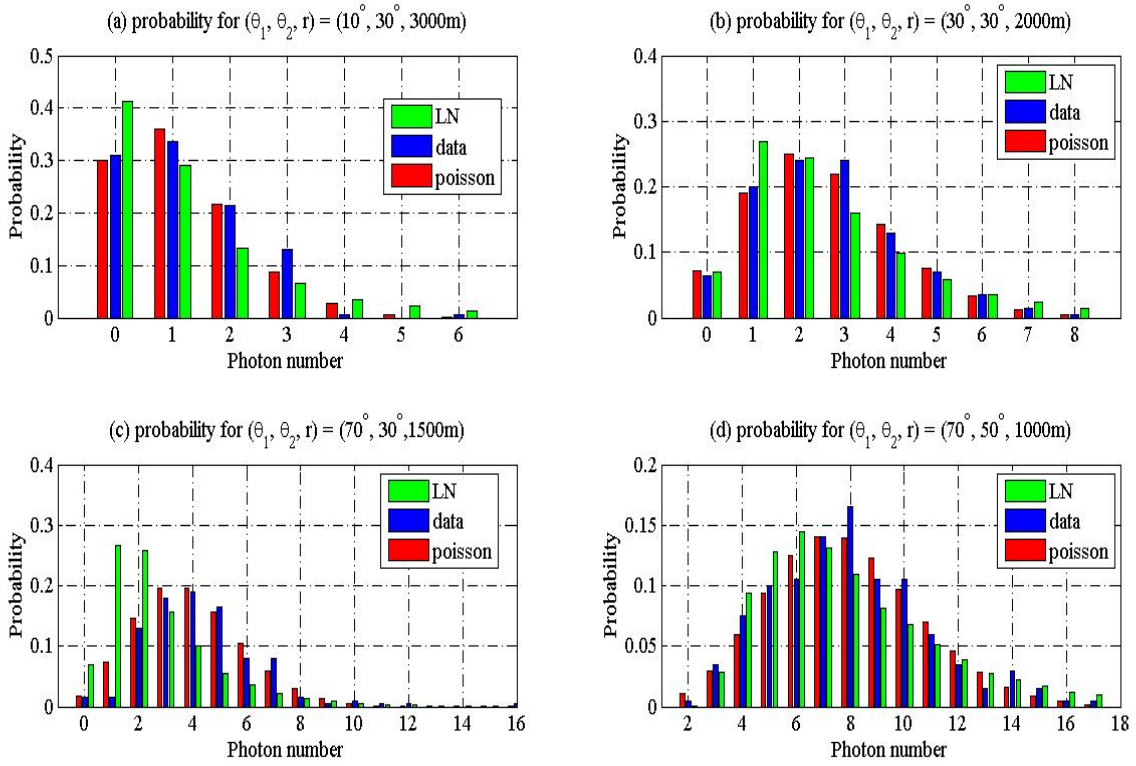

Figure 3.7: Comparison of model predictions and experimental estimates of photon count distributions for four system geometries.

to variation in the received counts. Therefore, Poisson PDFs is also plotted as comparison. Clearly, the Poisson PDFs appear to fit the data better than the PDFs based on the turbulence model. To quantify how well the PDFs of each theoretical model match the experimental data, Kullback-Leibler (KL) divergences were computed and are presented in Table 3.1. In all cases, the KL divergence between the Poisson PDFs and the measured PDFs are less than the corresponding divergence for PDFs based on the turbulence model, with the greatest difference corresponding to Fig. 3.7(c). As such, it appears that the effects of turbulence (if such effects exist) on the count distributions may be overwhelmed by shot noise. However, with limited sample sizes, the conclusions that can be drawn from this data

Table 3.1: Kullback-Leibler divergence comparison for the data presented in Fig. 3.7

	Figure 3.7(a)	Figure 3.7(b)	Figure 3.7(c)	Figure 3.7(d)
LN	0.06041285	0.028795359	0.135234679	0.037581134
Poisson	0.01429303	0.00204779	0.029061495	0.012825559

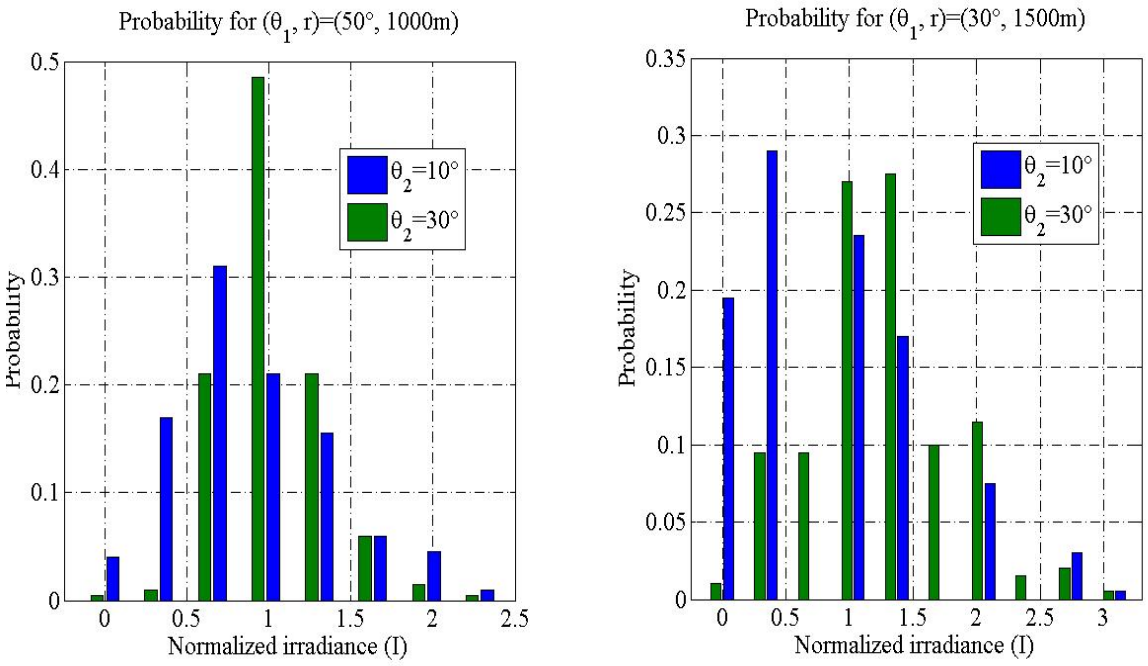

Figure 3.8: Comparison of the irradiance PDFs as the receiver elevation angle increases in two representative system configurations.

set may be restricted, so further research into the turbulence modeling is encouraged.

Finally, it is stated in [34] that the incorporation of more potential propagation paths from the transmitter to the receiver might mitigate turbulence effects, which could, for example, result in the reduction of irradiance fluctuations. A possible implication is that reduced turbulence effects may be observed for system configurations with a large common volume. Figure 3.8 provides some experimental evidence to support this inverse relationship. Each subfigure compares the normalized irradiance PDFs as the receiver

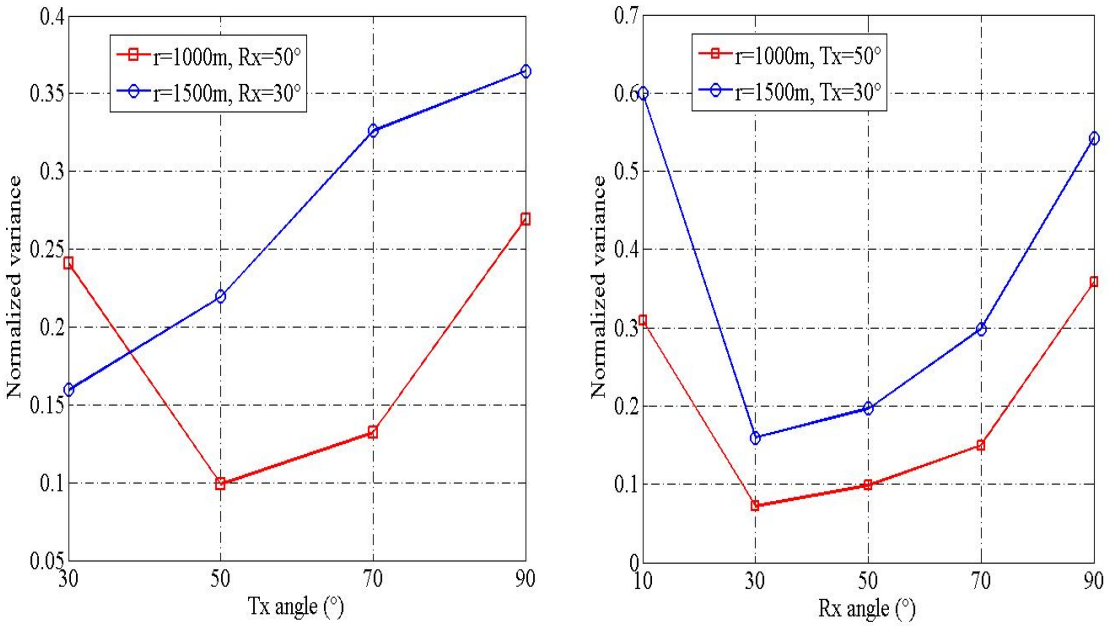

Figure 3.9: Normalized variance of the received irradiance for various system geometries.

elevation angle is increased while all other system parameters are held constant. An increase in the elevation angle results in a larger common volume and a reduced variance in the irradiance distribution. However, we note that the above effect does not appear to be monotone in the elevation angle. This is shown in Fig. 3.9, which depicts the normalized variance of the received irradiance for various system geometries. This complex behavior is not sufficiently explained by existing turbulence modeling approaches, suggesting the need for model refinement.

3.5 Predicted Communication System BER Performance

The bit error rate (BER) for a NLOS UV communication system depends on several factors, such as modulation scheme, detector type, transmitted power, path loss, data rate, and background noise. In this section, we restrict our attention to on-off keying (OOK) with direct detection and provide predictions of the BER performance for a system corresponding to the devices employed in our channel measurement experiment. According to the results in Section 3, the received pulse width is expected to be less than 10 μs when the range is less than 2000 m. Therefore, we assume that intersymbol interference is not a factor for the system being considered with a data rate of R =100 kbps at a range of 2000 m or less.

Given a noise count rate of N Hz, a receiver will detect a mean of $\lambda_{\mathrm{n}} = N/R$ counts per transmitted "0" and a mean of $\lambda_{\mathrm{s}} + \lambda_{\mathrm{n}}$ counts per transmitted "1," where λ_{s} is the mean signal counts per transmitted pulse. Assuming Poisson count distributions, the system bit error rate is given by $\mathrm{BER} = \left[1 - F_{\lambda_{\mathrm{n}}}(\tau) + F_{\lambda_{\mathrm{s}}+\lambda_{\mathrm{n}}}(\tau)\right]/2$, where $\tau = \lfloor \lambda_{\mathrm{s}} / \ln\left(1 + \lambda_{\mathrm{s}}/\lambda_{\mathrm{n}}\right) \rfloor$ is a decision threshold, F_{λ} is the Poisson cumulative distribution function with parameter λ, and $\lfloor x \rfloor$ denotes the greatest integer less than or equal to x. For the case of negligible noise ($\lambda_{\mathrm{n}} \approx 0$), the BER simplifies to $\mathrm{BER} \approx (1/2)e^{-\lambda_{\mathrm{s}}}$.

Based on the experimental path loss results, Fig. 3.10 shows BER performance predictions assuming negligible noise for three sets of pointing angles (θ_1, θ_2): (30°, 30°), (50°, 50°), and (70°, 70°). For the system parameters considered here, it is apparent that long-distance communication is only marginally achievable for extremely elevated pointing angles. However, at low but reasonable pointing elevation angles, an effective communica-

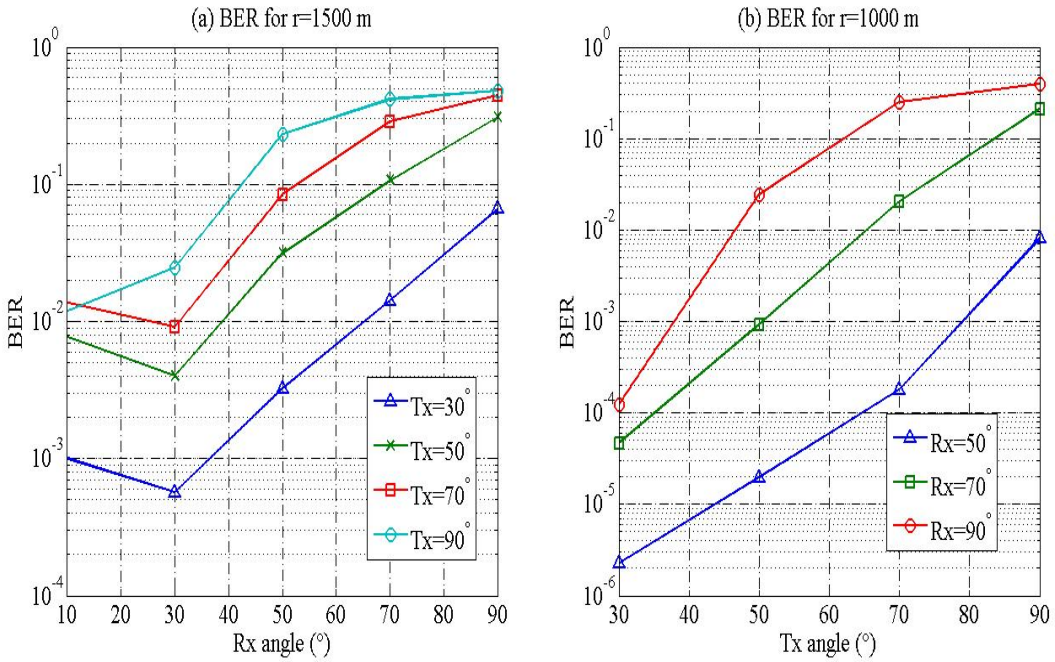

Figure 3.10: Predicted BER based on experimental path loss measurements.

tion link can be achieved at a range of a kilometer or more.

Next, Fig. 3.11(a) illustrates the predicted BER performance, again based on the experimental path loss results and assuming negligible noise, as a function of range for a transmitter elevation angle of 30°, 50°, or 70° and a vertically pointed receiver. The sensitivity of the performance of NLOS UV communications to range for these geometries is apparent from the figure. For instance, when the transmitter elevation angle is 30°, the predicted BER increases from 10^{-12} to 500 m to 10^{-4} at 1000 m. Lastly, Fig. 3.11(b) demonstrates the impact of noise on BER performance for three sets of system geometries, where the considered noise count rates range from 0 (noiseless) to 50 kHz (extremely strong). The potential for performance improvement that might be achieved through noise reduction

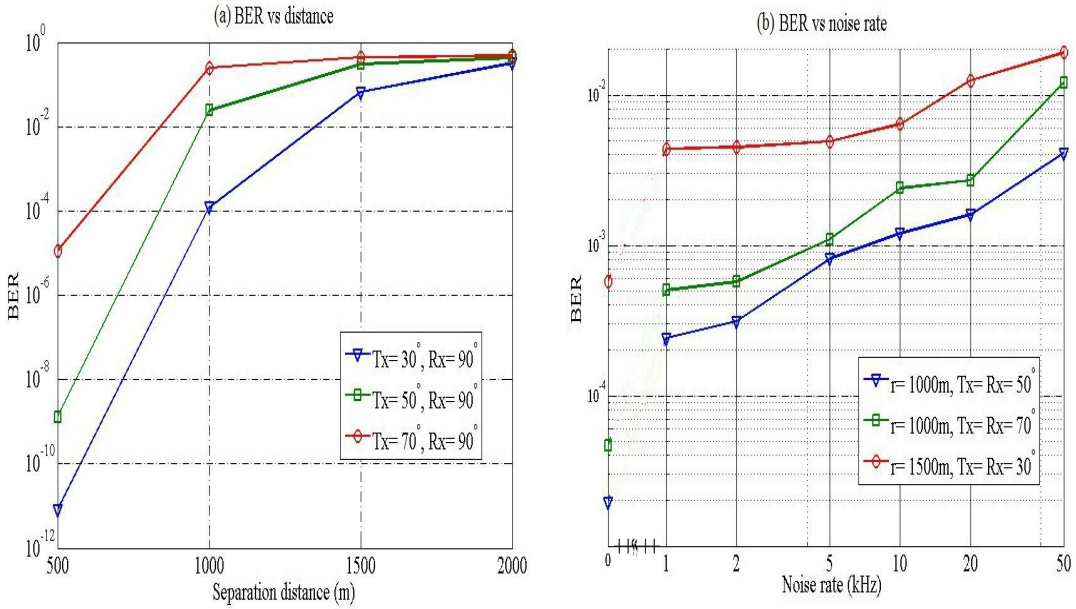

Figure 3.11: Predicted BER based on experimental path loss measurements.

with optical filtering and/or the use of detectors with low dark count is clear from these BER curves.

Finally, it should be noted that the measurement system employed here transmitted one pulse per second. A communication system that is to communicate at higher rate (e.g., the 100 kbs assumed in this section) with the same energy per pulse would be required to output proportionally higher power, which can be a severe practical constraint. Hence, this study highlights both the potential of and challenges associated with NLOS UV communications.

3.6 Summary

We reported on a recent data collection experiment in which a variety of channel-sounding measurements were taken to characterize various aspects of long-distance NLOS UV communications. In particular, analyses of measurements of path loss, pulse broadening, and photon-count distributions were presented and compared with previously developed theoretical channel models. Using the experimental path loss measurements, we also considered the BER performance of a representative long-distance NLOS UV communication system.

Predictions from a Monte Carlo propagation model are in reasonable agreement with several of the experimental measurements, providing validation of this modeling approach. However, the path loss measurements do exhibit mismatch with this channel model, which generally under predicts the observed path loss. This mismatch might be attributable in part to tolerances in device specifications, but other possible sources of additional channel attenuation should be considered. For example, we presented path loss estimates incorporating turbulence-induced attenuation (as predicted by previously developed turbulence modeling) that exhibit reduced error with respect to the path loss measurements. However, model predictions of other turbulence effects, such as a log-normal distribution of received photon counts, do not appear to be supported by the experimental data, suggesting the need for model refinement. In any case, our experimental and analytical results further the fundamental understanding of the long-distance NLOS UV channel, an essential prerequisite to the design of effective long-distance NLOS UV communication systems.

Chapter 4

UV LED array based NLOS UV turbulence channel modeling and experimental verification

4.1 Introduction

As communication range and the index of refraction structure parameter increase, optical turbulence in the UV-C band may deteriorate the communication system performance with the effects of irradiance fluctuation (scintillation) and extra signal attenuation. Thus, author in [17] proposed an analytical model of NLOS UV turbulence channel for the first time. In paper [18, 19], authors advanced the previous model and took extra turbulence attenuation into account. Both of those two models, however, were limited because they assumed that the photons were only scattered once before detected by the receiver.

In this chapter, we propose a MC channel model to capture the multiple scattering channel behavior under turbulence condition. In addition, we present a serial experimental results and study the characteristic of NLOS UV turbulence channel with farthest distances up to 1 km. Through the experiment and simulation, we discuss the turbulence effect on NLOS UV channel with focus on received-signal energy distribution and channel path loss. In a addition, a special characteristic of NLOS UV channel is proposed and studied as well, which is turbulence strength trade off between path length and common volume size. To the best of our knowledge, this is the first experiment to study NLOS UV turbulence channel characteristic.

4.2 NLOS UV Turbulence Channel Model Based on Monte Carlo Method

With the increasing of communication distance, optical turbulence effects may degrade UV communication performance because the fading irradiance significantly deteriorates the received signal in two aspects: received energy fluctuation and extra average path loss. According to the Rytov solution to the wave equation, the log-amplitude variance is proportional to $\lambda^{-7/6}$ [**?**]. As a result, the irradiance fluctuations due to atmosphere turbulence might be two or three times worse in the UV band than in the visible or infrared (IR) band, implying that UV links may be much more sensitive to turbulence compared to other optical links.

However, few analytical or numerical channel models have considered the NLOS turbulence effect comprehensively. In this work, we extent previous MC multiple scattering

channel [**?**] and introduce some critical parameters for turbulence channel. Fig. 4.1 depicts the scenarios of multiple scattering. For weak and moderate turbulence, each LOS part

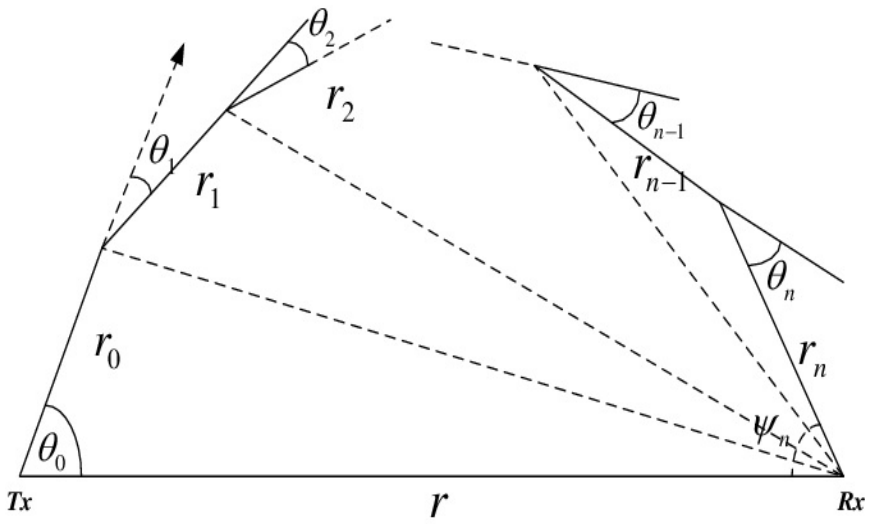

Figure 4.1: Photon migration path for n scatterings

irradiance has a LN pdf. We also use monte carlo method to simulate this whole complex progress. The photon trajectory is then simulated by successive migration paths among different scattering centers in the channel. However, turbulence has typically been ignored in UV NLOS link models, which usually focus on relatively short ranges and clear weather conditions where scattering and absorption effects may dominate. Assuming there are n times of scattering, one n time NLOS path is comprised of $2n$ segments, including n paths from the transmitting point to the scattering centers and n paths from scattering centers to the Rx. Given each scattering is self-governed, and the distances and angles for different scattering events are dependent on previous quantities. Therefore, on each segment, the photon's propagation is assumed to follow the law of single scattering until it reaches the

next scattering center or arrives at the receiver. Following this theory, the distance between each scattering interaction is given by the random variable:

$$\Delta s = -\frac{ln\epsilon^{(s)}}{k_s}, \tag{4.1}$$

where $\epsilon^{(s)}$ is a uniform random variable between zero and one, and k_s is the scattering coefficient. In addition to scattering, the NLOS UV communication is also affected by turbulence. By takeing advantage of that UV LED array is a non-coherent source and each scattering center is spatially separated, each scattering center can be regarded as a secondary point source emitting photons independently so that we can apply the turbulence theory to each LOS path. According to the Rytov approximation [20–21], the scintillation attenuations (dB) of each LOS path can be expressed as

$$\alpha_{\Delta s} = 2\sqrt{23.17C_n^2(2\pi/\lambda)^{7/6}\Delta s^{11/6}}, \tag{4.2}$$

where C_n^2 is the index of refraction structure parameter, which is altitude dependent. The typical value of C_n^2 is 10^{-13} $\mathrm{m}^{-2/3}$ for strong turbulence, 10^{-15} $\mathrm{m}^{-2/3}$ for medium turbulence, and 10^{-17} $\mathrm{m}^{-2/3}$ for weak turbulence, respectively. Thus, the corresponding turbulence attenuation of each path in linear scale is

$$L_{\alpha_{\Delta s}} = 10^{-\alpha_{\Delta s}/10}. \tag{4.3}$$

where Δs can be calculated from (4.1).

As well as additional signal attenuation, optical turbulence effects may also lead to irradiance fluctuations. According to our experience and field test results, there is an obvious turbulence effect once the baseline distance is over 200m and the atmosphere circumstance

is approximately assumed to be weak-medium condition. Therefore, here we adopt log-normal (LN) distribution to describe the probability density functoin (PDF) of LOS received intensity. With the irradiance denoted by I, the log-normal model distribution is given by following:

$$p_T(I) = \frac{1}{I\sqrt{2\pi\sigma_{\mathrm{l}}^2}} \exp\left\{-\frac{[\ln(I/I_0) + \sigma_{\mathrm{l}}^2/2]^2}{2\sigma_{\mathrm{l}}^2}\right\}, \tag{4.4}$$

where I_0 stands for the mean of received irradiance and variance of the log amplitude fluctuation σ_l^2 is defined as follows:

$$\sigma_l^2 = 1.23 C_n^2 k^{7/6} \Delta s^{11/6}, \tag{4.5}$$

for a plane wave, where k is the vector wave number $(2\pi/\lambda)$.

Without turbulence, the w, arriving probability of each photon, can be obtained by the simulation process described in [5]. However, when taking turbulence effect into account, the arriving probability of each photon in the arriving scattering center should scale a linear scintillation attenuation $L_{\alpha_{\Delta s}}$ and random irradiance variable T, as shown by:

$$w = w \times L_{\alpha_{\Delta s}} \times T, \tag{4.6}$$

where T follows the distribution (4.4). By merging those above mentioned critical variable into the MC based channel model in [5], the entire photon's immigration behavior under the turbulence circumstance can be captured. Next, we apply this model to obtain all the simulated numeric results and use a serial of experiment to verify this new model in following section.

4.3 Experiment Test Bed, Setup Condition and Methodology

In order to observe the obvious turbulence effect, we conducted a series of experiment from June 20, 2014 to June 23, 2014 during the daytime hours from 9 am to 9 pm. According to the weather records, the outdoor temperature ranged from 17.2° C to 33.3° C. The average wind speed during the testing was from 3.5 mph to 15 mph and the average relative humidity was 39.5%. Experiments were conducted in a flat open field of University of California, Riverside, which was located a significant distance away from any considerable optical noise sources (such as illumination devices). All of the measurements reported here were collected by utilizing a collimated UV LED array test-bed shown in Fig. 4.2.

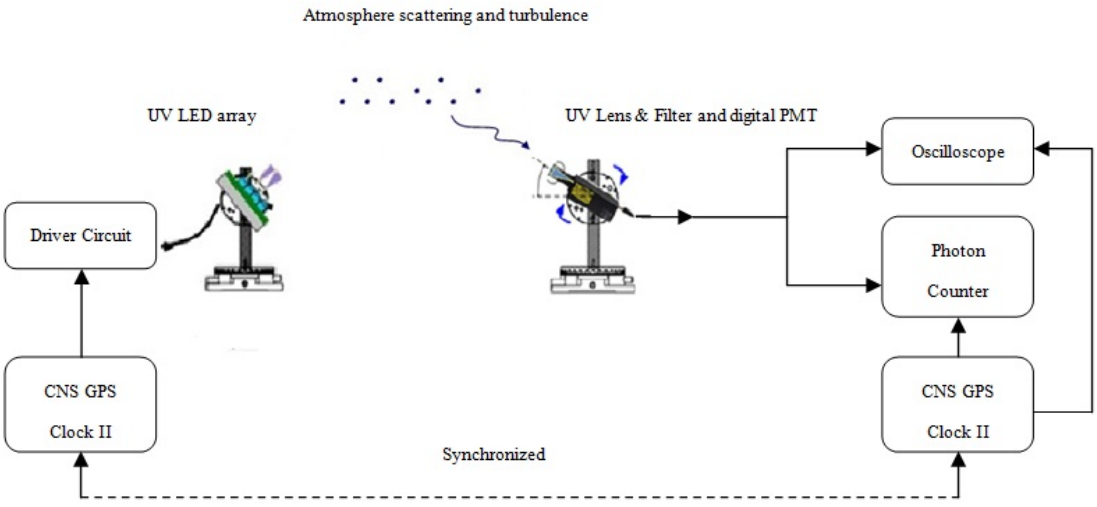

Figure 4.2: NLOS UV channel measurement system.

At the transmitter side, a 6-pact 270 nm UV LED array was deployed with 1.8 mW average output optical power. On the top of each LED, we put a collimation lens to make the output full beam angle within 1°. The transmitting pulse width was set to 1 ms, ensuring enough photons were output from LED. Since high pointing angles geometries would bring a high mount of path loss and the output power of LED array was limited, we only used UV LED array to conduct the measurements on low pointing angles cases. Based on our simulation and observation, there was no saturation issue [26] occurred in our testing cases.

Synchronization between the transmitter and the receiver was achieved via two synchronized GPS CNS II clocks that each output one 100 pulse per second (100 pps) signal. Since the frequency of atmosphere turbulence is very close to the GPS rate, each transmitted signal can be regarded as independent instance. At the receiver side, with a 15% efficiency 270 nm solar-blind filter on top, a PerkinElmer MP1922 photomultiplier tube (PMT) was deployed, which output a standard transistor-transistor-logic pulse when a photon was detected. It was responsive to wavelengths from 165 nm to 320 nm with 10 dark counts per second. The peak quantum efficiency of 15% and the peak gain of 10^6 occurred at a wavelength of 200 nm. The quantum efficiency decreased to 10% at 260 nm and 7% at 280 nm. The noise level of this PMT is under 10 count per second. Assuming 15% efficiency for filter and 10% quantum efficiency for PMT can be reached, another attenuation 18.24 dB was taken into account in our calculation. The digital PMTs had a circular sensing window with a diameter of 1.5 cm (resulting in an active area of 1.77 cm^2). Based on measurements, the effective field of view (FOV) of each detector (combining the PMT, solar blind filter, and attenuation filters) was estimated to be 30°. The resulting signal output from PMT

was recorded by MSA300, a high-speed photon counter with minimum 5 ns counting time and zero dead time, triggered by the GPS clock with an appropriate propagation time delay, which can be observed from the oscilloscope.

4.4 The Study of NLOS UV Turbulence Channel through Simulation and Experiment

In order to roughly quantify how turbid the atmosphere was, before each geometry data collecting, we first measured the LOS signal and then fitted the received-signal distribution to a log-normal (LN) distribution with C_n^2 as the only variable. By this, we can get the estimated values of C_n^2 at that moment, which are presented in below table. To make our simulation more accurate, those data estimated C_n^2 values will be adopted as reasonable parameters in following simulation.

Table 4.1: Estimated C_n^2 based on field test data

Distance (m)	300m	400m	500m	600m
C_n^2 ($m^{-2/3}$)	5.1×10^{-15}	7.01×10^{-15}	1×10^{-15}	6×10^{-15}
	700m	800m	900m	1000m
	2×10^{-15}	3.51×10^{-15}	1.8×10^{-15}	1×10^{-15}

4.4.1 Irradiance Fluctuations PDF

Due to the lacking of enough sample size, paper [35] could not give out a solid conclusion about the received energy distribution. Thus, to ensure enough sample size, we transmitted 1000 pulses in each configuration, in which the pointing angles are low. Then

we collected the received photon number of each pulse and use them to plot the PDF of normalized received energy.

Figure 4.3 (a) and (b) present two groups of original normalized field test results. Their configuration parameters are (r, θ_1, θ_2)=(400m, $10°, 10°$) and (r, θ_1, θ_2)=(350m, $10°, 15°$), respectively. For comparison, we also plot the corresponding fitting curves of experimental and simulated results in Fig. 4.3(c) and 4.3(d). It can be seen that the ex-

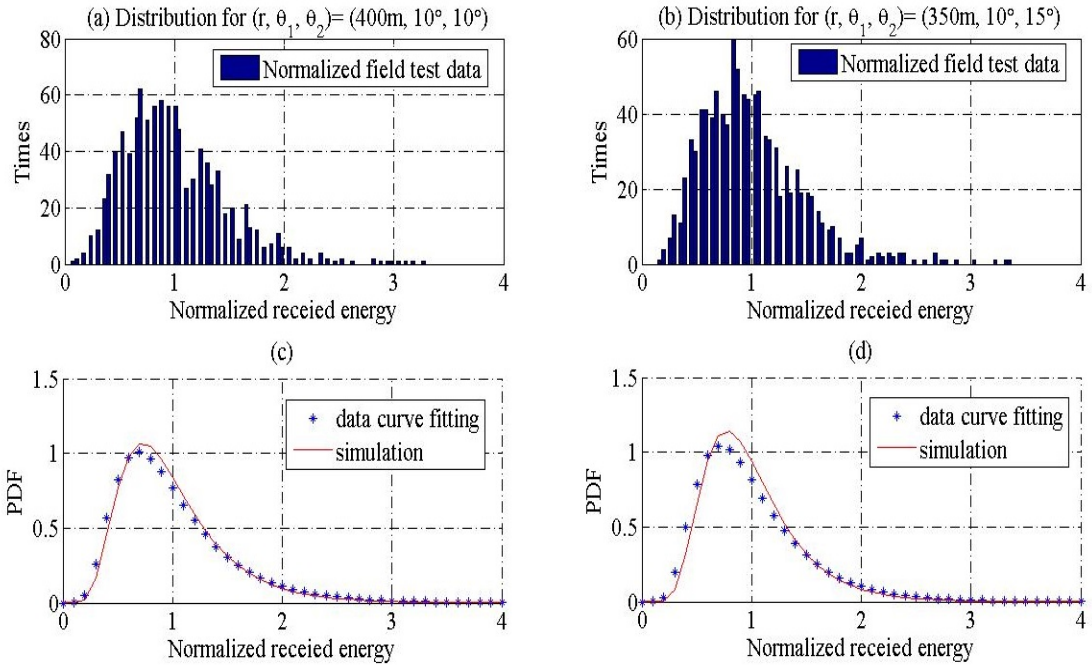

Figure 4.3: Field test results and the comparison between data curve fitting and simulation

perimental results and simulated results are very close and the general features appear to be captured by the proposed model, although there are some small mismatch between the theoretical and measured PDFs in those specific cases. These experimental and simulated results prove that the received-signal also follow LN distribution even in NLOS scenarios when the pointing angles are low and the atmosphere is in weak-medium turbulence con-

dition. Based on this, we predict that if the turbulence is very strong, the received signal might follow Gamma–Gamma distribution or K distribution.

Limited by our LED output optical power, we cannot receive enough photons to draw a figure with enough sample size when the pointing angles are relative high. In that cases, the number of received photon would drop into Poisson domain and dominated by shot noise. But if enough photons can be detected by the receiver, LN distribution will play a more significant role demonstrated by our results.

4.4.2 Turbulent NLOS UV Channel Path Loss

Since UV LED has more stable output optical power and higher bandwidth than UV laser, we can obtain more accurate path loss results with less time by using UV LED array. Therefore, in our experiment UV LED array was used to measure the turbulence NLOS UV channel path loss. Note that each measured received-energy exhibits random variations due to the probabilistic nature of the received signal. This can be especially problematic in configurations where the detected signal is weak, resulting in large differences between each measurement. As such, we averaged over 1000 realizations per geometry in order to obtain an accurate average path loss for each configuration.

Our previous work mainly focus on the average path loss without turbulence effect. But once taking it into account, the extra path loss become significant and can not be ignored. To investigate whether turbulence effect plays impact on the overall path loss, we conducted the experiment at different time, but with same system configuration. Figure 4.4 shows two groups path losses measured on daytime and nighttime respectively. Two groups

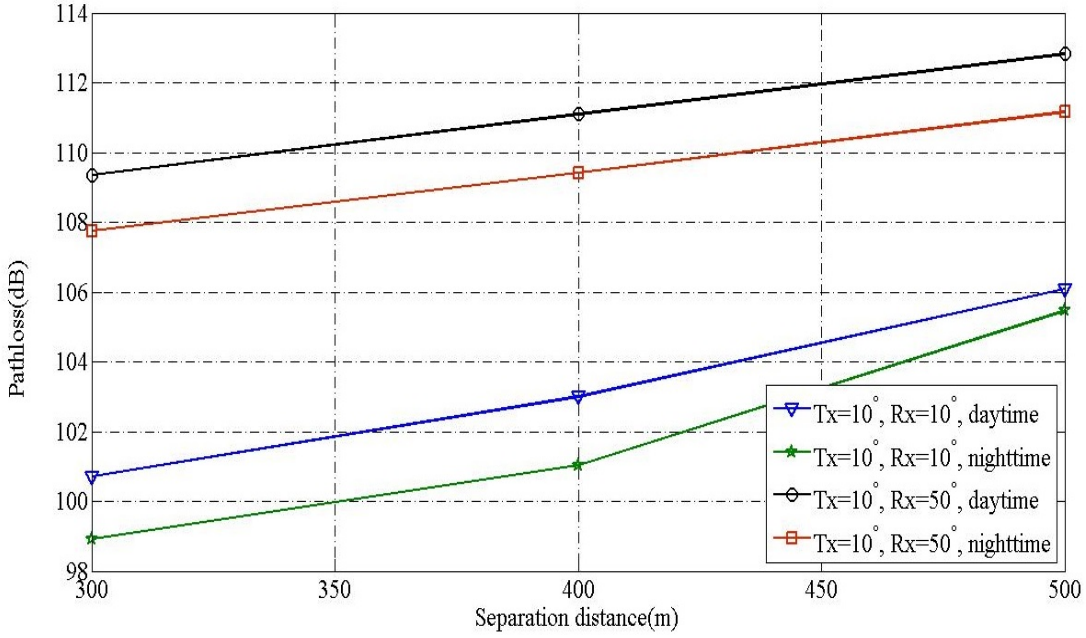

Figure 4.4: Difference of daytime and nighttime pathloss

system configuration is (θ_1, θ_2)=$(10°, 10°)$ and (θ_1, θ_2)=$(10°, 50°)$ and the baseline distance ranges from 300m to 500m. Except for the time, all the other system parameters were set as the same. Clearly, the path losses measured on nighttime appear to be 1–2 dB less than the results measured on daytime. The reasonable explanation is that the turbulence effect in daytime was stronger than in nighttime. So the daytime corresponding turbulence attenuation was greater than nighttime turbulence attenuation, resulting in the gap of 1–2 dB. Those experimental result prove the hypothesis we made in the beginning—-turbulence effect has an effect on overall channel path loss.

Then, to study how turbulence strength affects the link path loss, we then simulated the path losses with different C_n^2 (from 10^{-16} $m^{-2/3}$ to 10^{-14} $m^{-2/3}$) and the path loss without turbulence. The simulated results are presented in Fig. 4.5, as well as the field

test results as their comparison. As we can see, in both Fig. 4.4(a) and 4.4(b), the path loss presented by curve with $C_n^2 = 10^{-14}\ m^{-2/3}$ is apparent higher than field test results, as well as other simulated curves. And in those two testing cases, the curves of the medium turbulence condition ($C_n^2 = 10^{-15}\ m^{-2/3}$) show extremely fitness to the field test results. Obviously, the simulated path loss results with weak turbulence ($C_n^2 = 10^{-16}\ m^{-2/3}$) and those assuming no turbulence occurred are lower than the other curves. In a word, all the other curves unveil that the path losses would vary 2–10 dB on different turbulence conditions.

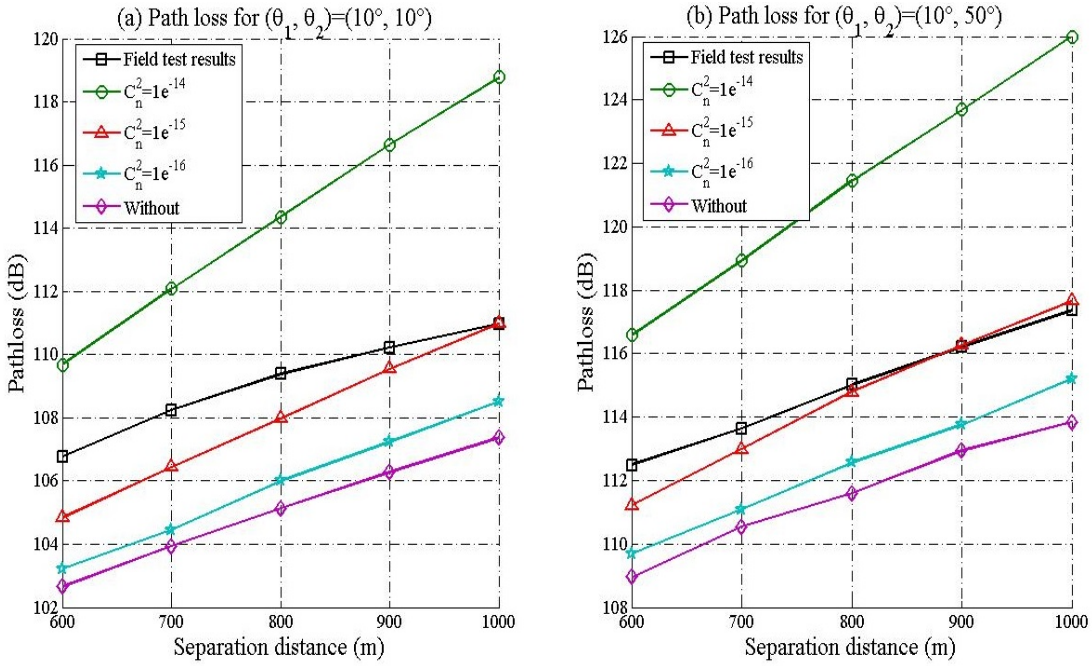

Figure 4.5: Nighttime path loss under different turbulence conditions

These measurements, along with their simulated results prove again that it is necessary to take turbulence attenuation effect into account when building the model to

estimate the NLOS UV channel path loss, as well as further system link budget estimation.

4.4.3 Study Special Characteristics of NLOS UV Turbulence Channel

The NLOS UV channel is a complicated stochastic process that it not only includes the atmospheric effect of scattering, absorption and turbulence. Different configurations of system and deployment positions will also lead to different channel responses. Through experimental and simulated data, we found a special characteristics of NLOS UV Turbulence Channel, which is the turbulence strength trade off between channel path length and common volume size. Therefore, next we further evaluate and analyze the received-signal scintillation distribution in terms of baseline distance and pointing angles.

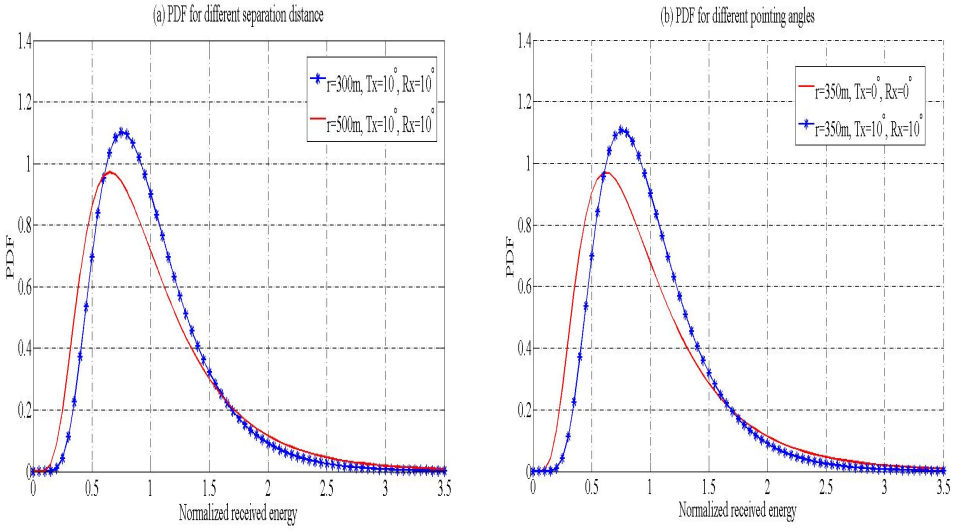

Figure 4.6: PDF of NLOS UV scintillation of field test results.

First of all, Fig. 4.6 once again prove the conclusion we get before that the received signal energy will follow LN distribution when turbulence is from weak to medium. The field test results in Fig. 4.6(a) depicts the PDFs of normalized received energy for NLOS UV links

with varying baseline range. The red curve (without asterisk) represents the PDF under the system configuration (r, θ_1, θ_2)=(500m, $10^\circ, 10^\circ$). As its comparator, the blue curve (with asterisk) shows the PDF under the system configuration (r, θ_1, θ_2)=(300m, $10^\circ, 10^\circ$). The only different system parameter is baseline distance. It appears that the signal will suffer more turbulence if it travels through longer channel. Obviously, the left flatter curve (the red one) deviates more from its mean than the other one. This phenomenon agrees with the LOS turbulence cases where the scintillation effect is proportional to the channel length. As such, stronger scintillation is supposed to be observed in a longer NLOS UV channel.

But Fig. 4.6(b) shows another interesting phenomenon and result, which doesn't comfort to this. The normalized received energy PDFs for the corresponding different pointing angles are illustrated by Fig. 4.6(b). In particular, all the system parameters are fixed except for the pointing angles for two representative geometries, (350m, $0^\circ, 0^\circ$) and (350m, $10^\circ, 10^\circ$). From the system configuration parameters, it's apparent that the channel length represented by blue curve (with asterisk) is longer than that represented by red curve (without asterisk). If applying the conclusion obtained from Fig. 4.6(a), the signal represented by blue curve (with asterisk) is suppose to appear more fluctuational than the signal represented by red curve (without asterisk). However, the normalized variance of red curve is 0.3652, which is larger than the other curve's variance, 0.1802. This observed phenomenon is opposite to what has been concluded from Fig. 4.6(a). And this mitigation effect is a special characteristic of NLOS UV channel. It is stated in [34] that the incorporation of the different potential propagation paths from the transmitter to the receiver has the potential

to mitigate the turbulence effects, resulting in, e.g., reducing irradiance fluctuations than previously predicted. Therefore, the bigger the size of common volume is, the more slightly the turbulence will affect the irradiance. Figure 4.6(b) provides experimental evidence to prove the existing of this phenomenon.

However, the above mitigation effect does not appear to be monotone as the change of pointing angles, illustrated by simulated results in Fig. 4.7, in which the normalized variances of the received-irradiance for various system geometries (here $\theta_1 = \theta_2$) are depicted. More specifically, the appearance of those curves look like to be concave and the minimum points are around at 20°.

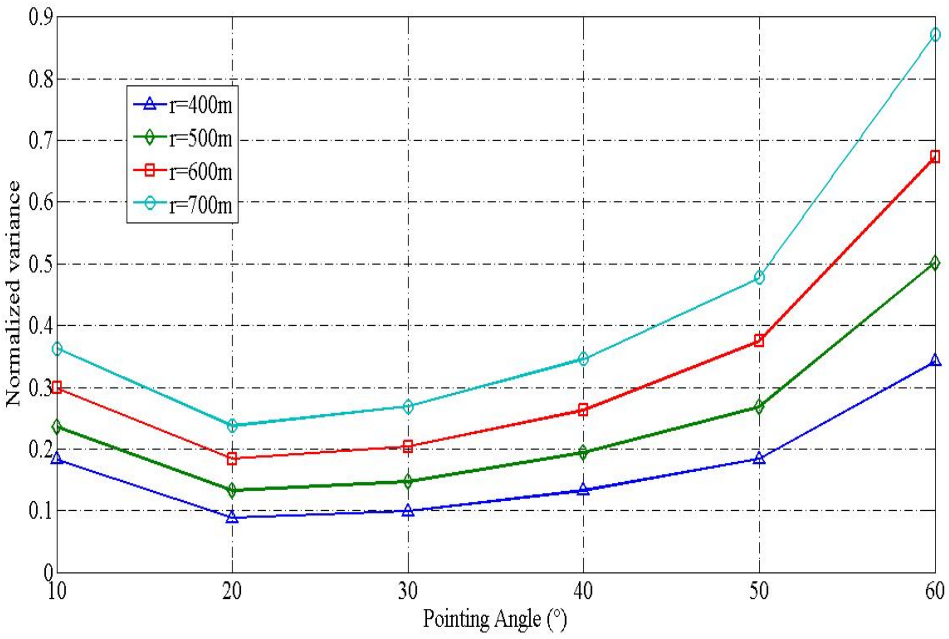

Figure 4.7: Normalized variance of the received irradiance for various system geometries.

Although the growth of pointing angles can enlarge the common volume size,

which leads that there are more paths for photons to reach the receiver, it also increases the channel length meanwhile. Therefore, the final received-energy distribution is a trade off between channel length and common volume size. Based on above simulated results, we reasonably predict that when pointing angles are in a certain range, the mitigation effect from common volume will overwhelms than the effect from the increase of channel length. However, if the pointing angles continue to grow, the scintillation effect will still improve in the end and turbulence effect caused by long channel length will dominate even with the mitigation effect.

When building a end-to-end NLOS UV communication, the choice of system geometry also becomes a trade off, because of this special characteristic. The system BER is related to two aspects: 1) average received signal energy, 2) received signal's variation. If we use low pointing angles, of course, the average received signal energy is stronger compared to high pointing angles. However, notice that higher average received signal energy might not lead to better system performance, because of stronger variation of signal. For higher pointing angles cases, it's opposite, less energy, but might more stabler. Therefore, in term of best end-to-end BER performance, the choice of best system geometry is still an open research topic.

4.5 Comparison Experiment-LED Array vs Laser

To observe the turbulence effect on high pointing angles cases, a high power compact Q-switched fourth-harmonic ND:YAG 266 nm laser that sent pulses with a nominal pulse width of 3 ns, and a 3 mrad full beam angle was used and deployed next to the LED

array. The test bed is shown in below picture. On high pointing angles cases, the laser signal suffered pulse broadening effect causing that the received-signal expanded to several microsecond, which made it possible for us to observe the received-energy distribution. If laser was used for measuring the low point turbulence effect, we would hardly see the obvious effect, because all the photons probably arrive at the receiver at very short time that over PMT's caught capability. The PMT will only response few number of photon, which cannot be used for observer. Therefore, for high point angles a UV laser is used with enough pulse broadening that reaches several microsecond in our scenario.

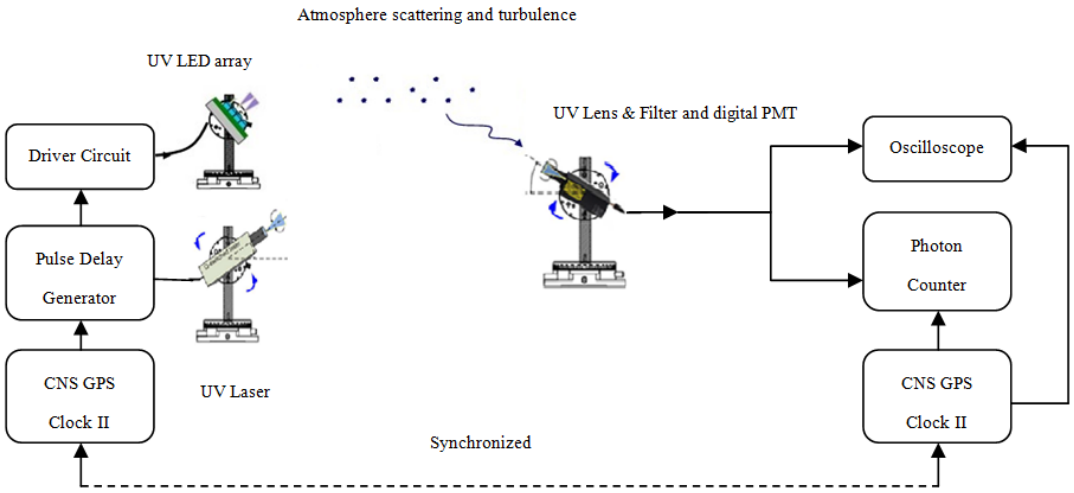

Figure 4.8: NLOS UV channel measurement system.

The laser was put into a cooling system because the daytime temperature was higher than the specified working temperature. The transmitter pointing angle was adjusted by using the combination of rotation stages with precise motorized angular control and an optical mirror. Although reflection cost some output energy, the laser still provided sufficient

energy for measurements on high pointing angles cases with average output energy 0.9 mJ, 1.2 mJ, 4.2 mJ on pointing angles 50°, 70°, and 90°, respectively.

As the pointing angles increased, the NLOS link caused huge path loss, so we used the UV laser as our optical source instead. Although the UV laser outputs very high energy, the pulse width is too narrow and the PMT can only respond few times in a pulse slot, even with pulse broadening effects. The shot noise of device and background noise dominated the distribution of the PMT output signal, as illustrated by the Poisson distribution shown by Fig. 4.9.

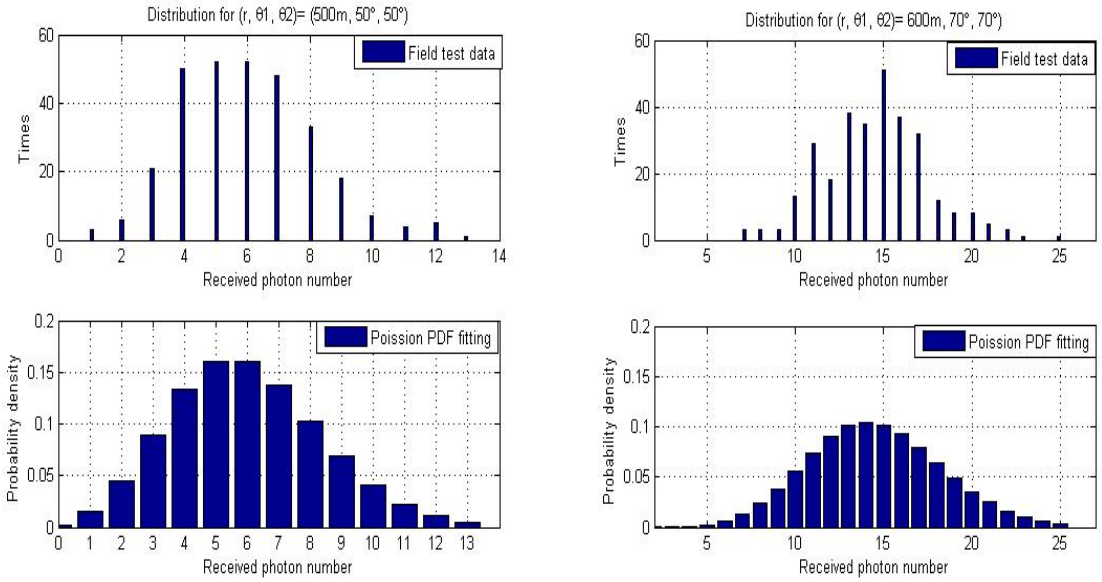

Figure 4.9: The field test result and curve fitting for UV laser.

4.6 NLOS UV Turbulence Case Study

Next, we further evaluated the received signal scintillation distribution by varying the optical pointing angles and baseline separation range. Fig. 4.10 depicts the scintillation

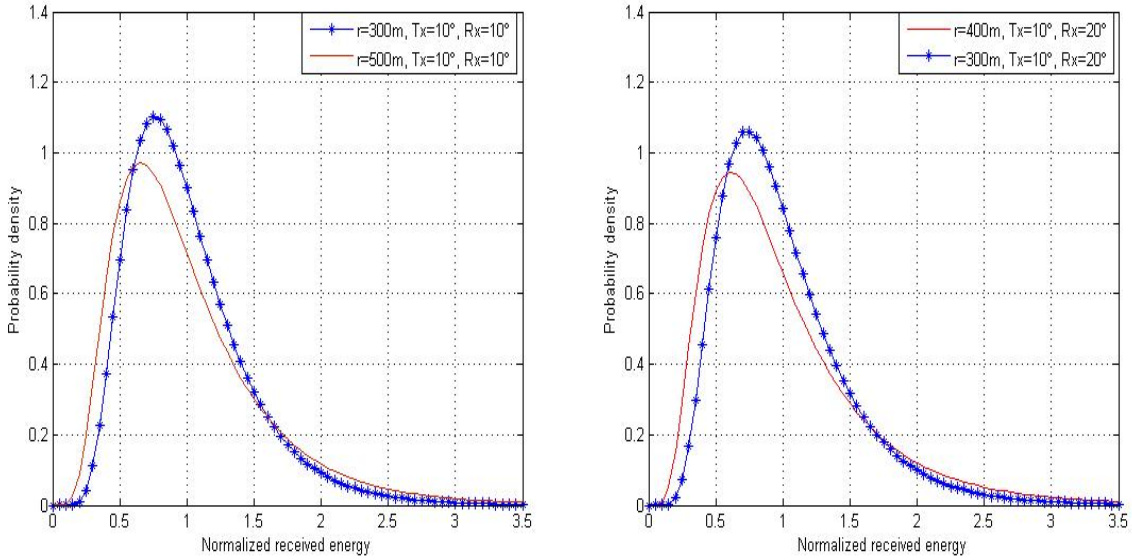

Figure 4.10: PDF of NLOS UV scintillation for varying separation range.

PDFs for NLOS UV links with varying baseline range. The longer the communication link, the more turbulence will affect communication performance. The curve is flat and skewed right, which means the variance of the distribution is larger than the other. For example, the variance of curve "r=300 m, Tx=10°, $Rx = 10°$" is 0.103, while the the other curve "r=500 m, Tx=10°, $Rx = 10°$"'s variance is 0.132.

The scintillation PDFs for the corresponding different turbulence conditions is illustrated by Fig. 4.11. In particular, with all the system parameters fixed except for the receiver elevation angles for two representative geometries, we observed that the irradiance

fluctuations vary with the size of the common volume. More specifically, with higher pointing angles, the received signal energy will fluctuate more than lower pointing angles. This field test result is opposite to the state in[34], which claims that the incorporation of the different potential propagation paths from the transmitter to the receiver has the potential to smooth the turbulence, resulting in reduced irradiance fluctuations for example. Therefore, existing NLOS UV turbulence modeling approaches still cannot predict the whole complex atmosphere behavior, which remains an open research area.

4.7 Predicted NLOS UV Communication System Performance

Modulation scheme, detector type, transmitted power, path loss, scintillation, data rate and noise are all the the significant factors impact the NLOS UV communication system bit-error-rate (BER). Following, We restricted our attention to on-off keying (OOK) with direct detection, and analyzed BER performance of the corresponding NLOS UV communication system. According to [36], the turbulence based BER is given by[36]

$$BER_{T,NLOS} = \frac{1}{2}\int_0^\infty f_y(y) erfc(\frac{< SNR_{T,NLOS} > y}{2\sqrt{2}})dy \tag{4.7}$$

where $f_y(y)$ is the received signal distribution, which can be obtained from MC channel model. The mean quantum-limit based signal-to-noise ratio (SNR) in the case of turbulence is expressed by $< SNR_{T,NLOS} >= \frac{SNR_{0,NLOS}}{\sqrt{\frac{P_{r0}}{P_r}+\sigma_y^2 SNR_{0,NLOS}}}$, where P_{r0} is the received power without turbulence, $< P_r >$ is the mean received power with turbulence, and $SNR_{0,NLOS}$ is the SNR in a NLOS communication link that assumes no turbulence. For simplified analysis, we assume that P_{r_0} is equal to $< P_r >$; $SNR_{0,NLOS} = \sqrt{\frac{y_0}{2Rhc/\lambda}}$, where y_0 is the

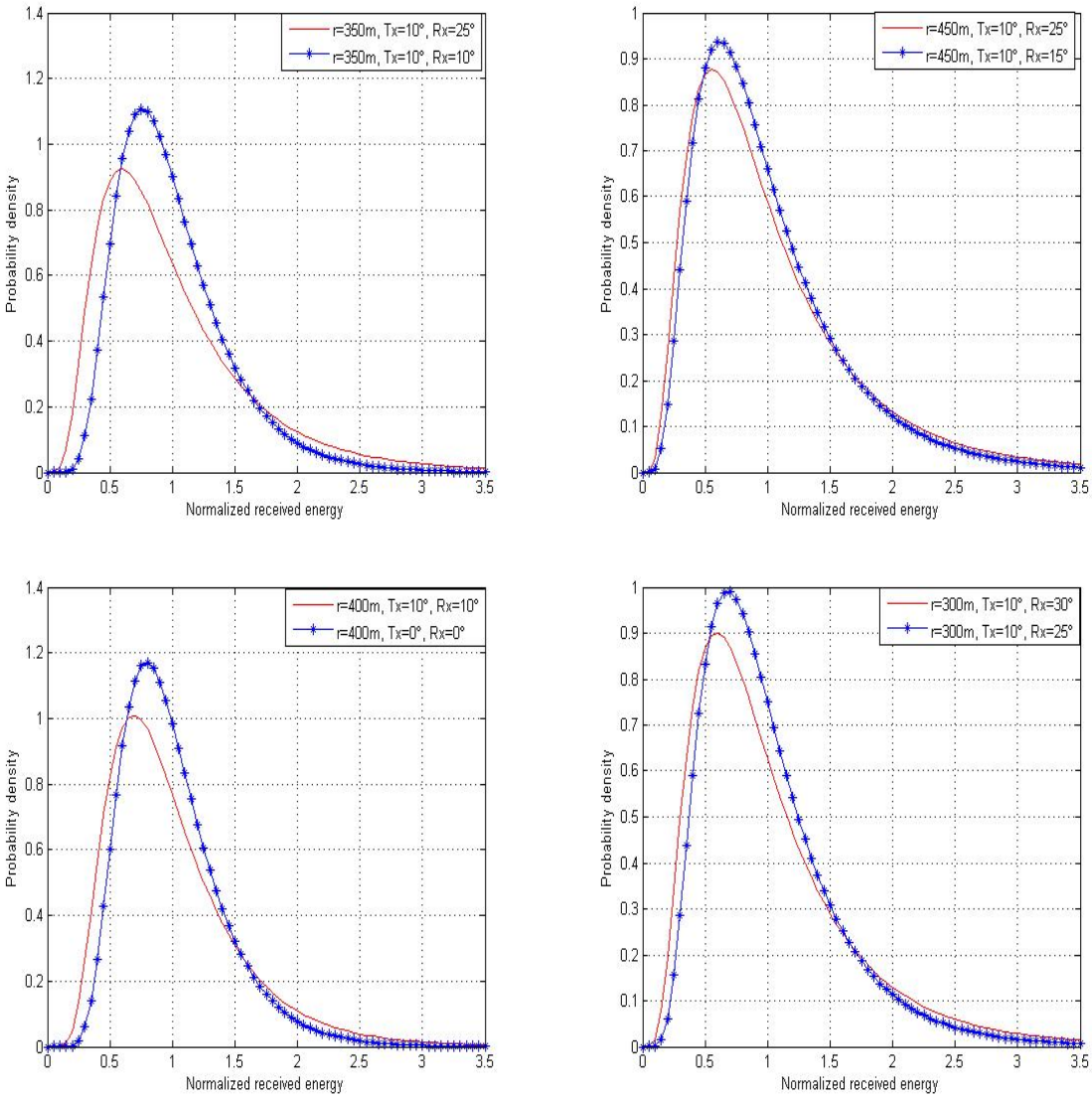

Figure 4.11: PDF of NLOS UV scintillation for varying pointing angles.

received power without turbulence and we assume it equals to received power y; R is the link data rate and the default value is $1kbps$ for our simulation; h denotes Plancks constant; c is the speed of light; and λ is the wavelength. The default transmitter is 100 collimated UV LED with $100 * 0.3e^{-3}$ output optical power.

To study how turbulence affect a NLOS UV communication system performance quantitatively, the separation distance, pointing angles, transmitting power were all taken into account as the crucial parameters. Figure 4.12(a) predicts rapid BER degradation

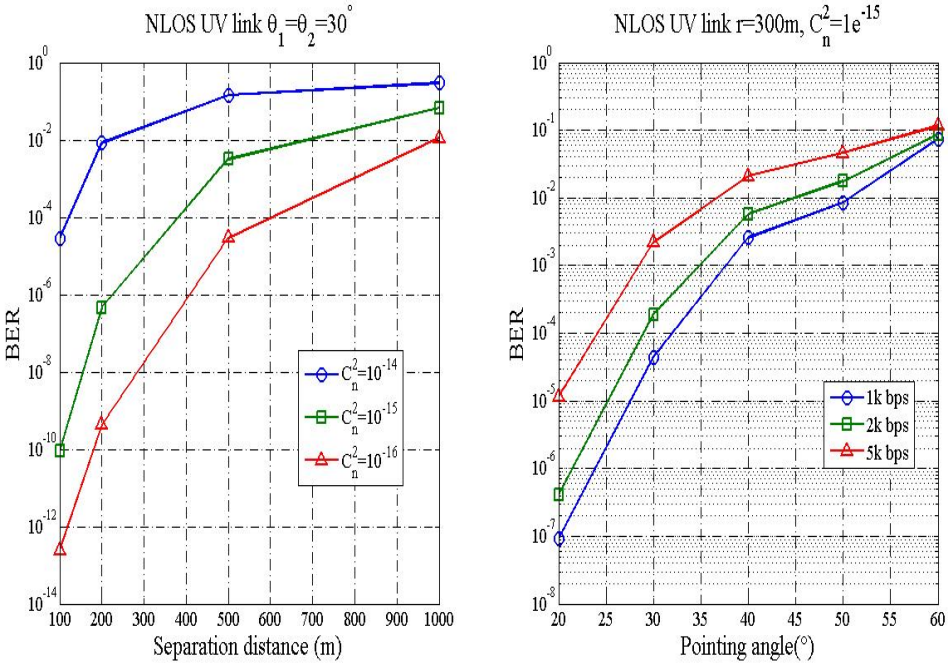

Figure 4.12: BER versus different system configurations in a turbulent NLOS UV link

with increasing baseline range when the baseline range changes from 100 to 1000 meters. Our calculations also show that the BER is very sensitive to the atmosphere structure parameter. For example, for atmospheric and geometry parameters (θ_1, θ_2)=$(30°, 30°)$,

r=500m, the BER of $C_n^2 = 1e^{-16}$ is far smaller than the BER of $C_n^2 = 1e^{-14}$. Figure 4.12(b) shows the BER performance of NLOS UV communication system with different pointing angles, varying from (θ_1, θ_2)=$(20°, 20°)$ to (θ_1, θ_2)=$(60°, 60°)$ under different system data rate.

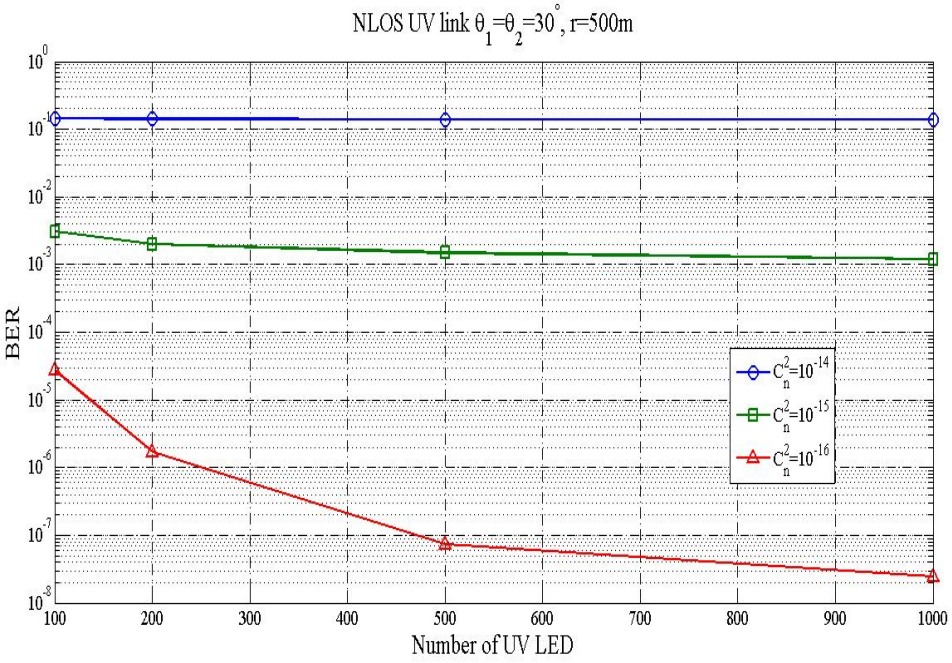

Figure 4.13: BER versus different numbers of UV LED

Figure 4.13 shows BER as a function of number of UV LED for different values of C_n^2. It can be seen that there are great BER deteriorations when the turbulence is high. For example, when the $C_n^2 = 1e^{-14}$, the BER is around 10^{-1}. Even though we increased the number of UV LED, the BER still cannot be improved. This is the same as to the situation when the $C_n^2 = 1e^{-15}$. However, through increasing the transmitted power, the BER performance can be improved when the turbulence condition is not high enough. This

figure also reveals that it's very difficult to obtain good BER performance through affording huge amount of UV LED when the signal is suffering strong turbulence effect. Instead, it implies that diversity techniques shall be adopted in NLOS UV communication to achieve reliable information transmission.

4.8 Summary

We conducted a series of measurements to investigate NLOS UV turbulence channel for the first time. The received-signal distributions and NLOS UV turbulence channel path losses were studied in terms of system geometry and turbulence strength. The comparison between experimental and simulated results provided the validation for the NLOS UV turbulence channel model based on MC method. Through field test data and simulation results, the received-signal energy is proved to follow LN distribution in NLOS scenarios when the pointing angles are low and the atmosphere is in weak-medium turbulence condition. In addition, we also prove that turbulence effect will induce extra path loss for NLOS UV communication. The special characteristic of NLOS UV channel was also observed and analyzed through experiment and simulation. Because of this special characteristic, the choice of system geometry becomes a trade off between the size of common volume and channel length. Those above experimental and simulated analysis is valuable to fundamentally understand the NLOS UV turbulence channel, which is an essential prerequisite to the design of a NLOS UV communication system.

Further open work in this area include the outdoor experiment and model verification under severe turbulence condition. Due to the special characteristic of NLOS UV

turbulence channel, the choice of best system geometry is still an open research topic.

Chapter 5

GPS synchronized NLOS UV communication system based on USRP

5.1 Introduction

In this chapter, we integrate Universal Software Radio Peripheral (USRP) into UV communication system and employ GPS as synchronized signal. At receive side, photon counting and adaptive threshold method are used to recover the original signal. Through experiments, we test the BER and path loss of the system under different configuration geometries, as well as some basic MAC protocols. Some initial results are compared to the previous proposed path loss and BER model.

Software defined radio (SDR), where the design flow is mostly in software, makes

it useful for fast prototyping of new communication techniques by leveraging the inherent flexibility of software based systems compared to their hardware-based counterparts. We apply Universal Software Radio Platform (USRP N210) as our SDR, which contains the hardware implementation units from baseband to the RF frontend, as well as one LFTX (DC-30Mhz) and one LFRX daughter board (DC-30Mhz). Two CNS Clock II are used for generating 10Mhz external reference clock signal and 1pps signal for synchronizing two separated USRP.

5.2 General system structure

Due to UV special communication channel, in some particular communication geometry only few photons arrive in one time slot, so phase and frequency information are hardly to be recovered in this scenario, while IM/DD (intensity modulated/direct detection) system still works. In this system, OOK modulation and photon counting demodulation are applied. All path loss and BER test results are based on a solar blind GPS synchronized UV communication system at 260 nm wavelength, which is shown in Fig. 5.1. At transmitter side, 2 ball-lens UV LEDs (TO-39) are driven by the amplified modulated signal out of Tx USRP, with 6.5V driving voltage and 60 mA driving current. Each LED gives out 0.3 mW optical power, with 7° beam angle. Through Linux software Gnu Radio, laptop A controls the USRP to generate corresponding signal. GPS servers as the external clock and supplies 10 Mhz reference clock and 1 pps trigger signal. At the receiver side, a commercial digital PMT (Perkin-Elmer photomultiplier tube) with a solar blind UV filter on top is deployed to convert the received optical signal to electrical signal. The PMT has a built-in current

preamplifier and with a circle sensing window with a diameter of 1.5 cm(resulting in an active area of 1.77 cm^2). It has a spectral response from 165 nm to 320 nm, 10 dark counts per second. The peak quantum efficiency of 15% and peak gain of 10^6 occurs at 200 nm, while decreasing quickly towards longer wavelengths, about 10% at 260 nm and 7% at 280 nm. Combining the solar blind filter and PMT, the detector's effective FOV (Field of View) is estimated to be 30° based on rough measurement. Another GPS at receive side acts as system clock as well. At last, Rx USRP demodulates incoming signal and then sends to laptop B.

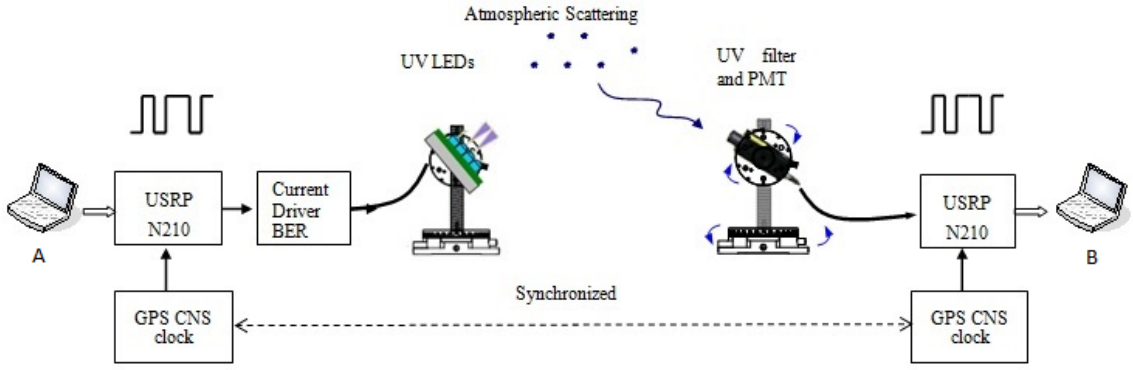

Figure 5.1: NLOS GPS UV USRP communication system diagram.

Based on previous experiment test[37], the photon width ranges from 20 ns to several microsecond in different configuration scenarios. Due to laptop and USRP's limitation, receive side USRP sample rate is only set to 25 Mhz, which is lower than the narrowest photon width. Therefore, the communication link cannot be built when the signal strength is too weak.

To obtain path loss L, the ratio of transmitted and received power $L = P_t/P_r$,

received photon number is recorded to represent received power. It is impossible for a photon counter to record how many photons is transmitted (up to $3.9239 * 10^{10}$). Thus, a high performance power meter is employed to measure the emitted optical power. Each photon carriers energy hc/λ, where c is the light speed, h is Planck's constant, and λ represents wavelength. Consequently, transmitted photon number can be easily represent as $N_t = P_t T_p \lambda / hc$. In order to avoid the symbol jittering, we only choose the duration of symbol "1" to be 50%. The number of photons detected by the PMT per pulse is N_d, which is a percentage of the number of arriving photon number N_r, which is given by $N_d = \eta_f \eta_r N_r$, where η_f is the filter transmission efficiency and η_r is the PMT detection efficiency. Therefore, the path loss is defined by $10log10(\eta_f \eta_r P_t T_p \lambda / hc N_d)$ dB. Through GPS synchronization, Rx USRP keeps sampling in time domain to count photons and then makes decision.

5.3 The comparison and analysis between system performance and model prediction

In this section, we compare our experiment results to the simulation results and investigate the NLOS UV link performance by analyzing link path loss, system BER etc.

5.3.1 Link path loss

Given the power limitation of our experiment LED, we only focus on range from 5 meters to 30 meters. We examine the path loss while varying Tx and Rx apex angles. Due to special experimental circumstance, we estimate our experiment were under weather

condition from thick to extra thick, whose scattering coefficient can be found in Table 2.1.

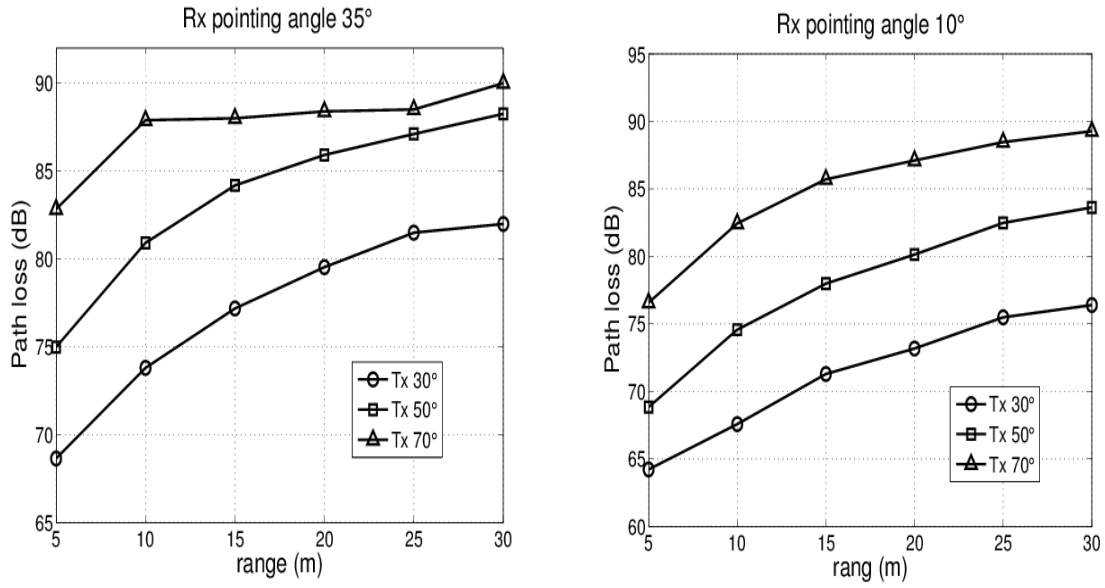

Figure 5.2: System path loss under different configurations.

Fig. 5.2(a) and 5.2(b) depict range-dependent path loss for varying Tx and Rx pointing angles. We can see that path loss is very sensitive to the Tx pointing angles. In particular, for fixing large Rx pointing angles increasing Tx pointing angle may exhibit dramatic path loss deterioration, which implies that it is necessary to increase the transmitted power to compensate the high channel attenuation loss for large apex angle geometry. Due to USRP sample rate's limitation and site's restriction, we only measure path loss up to 90 dB around.

Fig. 5.3(a) and 5.3(b) compare predicted path loss model with experiment results for Rx angle up to 40° when baseline separation is $10m$ with Tx angle 70° and 30°. We can see that empirical model describes path loss tendency well, especially in low pointing

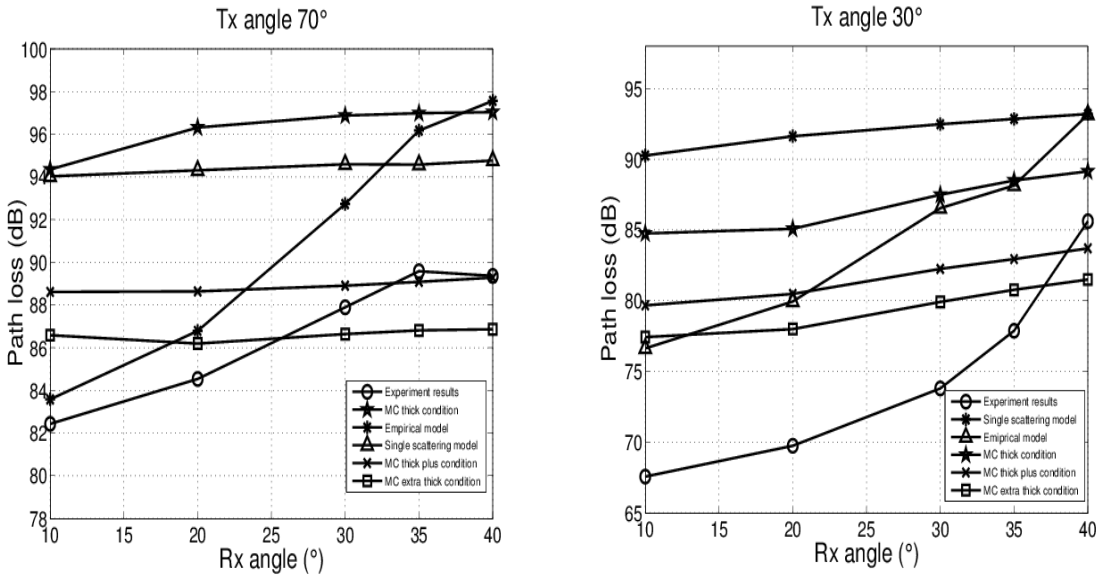

Figure 5.3: Comparison of measured and simulated path loss results.

Rx angle, but error rises as apex angle increase. Scattering coefficients also intensively impact path loss at short range. Different values of scattering coefficients will lead to 3-5 dB disparity. When both Tx angle and Rx angle are large, MC model's prediction is very close to tested results under thick plus condition, while it deviates from experiment results under low pointing angle. We believe those discrepancies is directly attributable to measurement distortion arising from the partial LOS signal detected by receiver with large FOV as baseline distance and Tx elevation angles are small. This also makes single scattering path loss model predict inaccurate. What's more, it misses the multiple scattering part, which is relatively high under present weather condition.

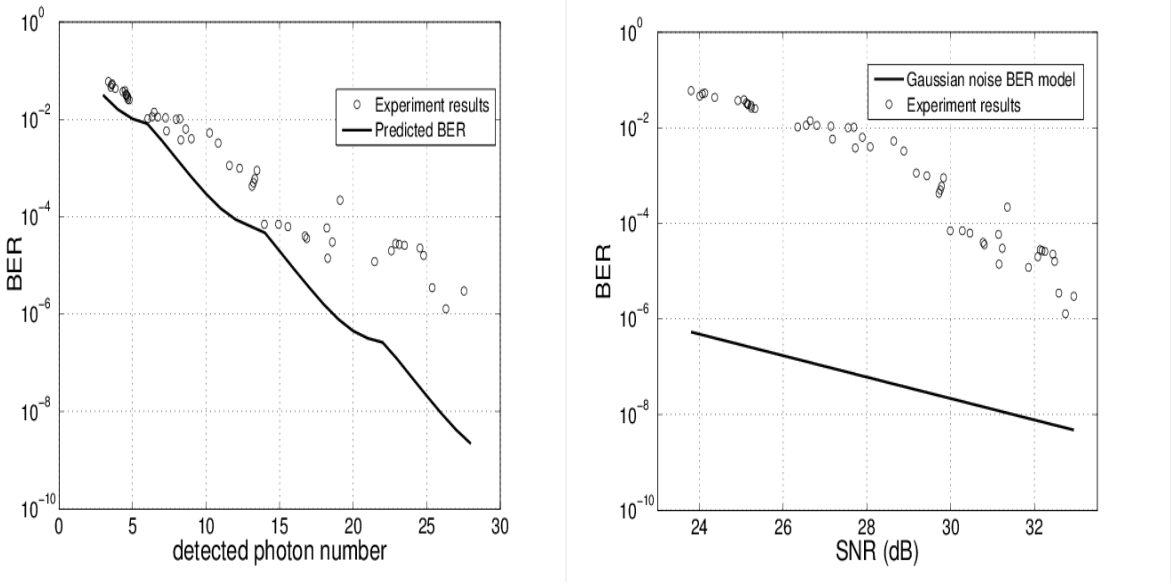

Figure 5.4: Comparison of measured and simulated BER results.

5.3.2 System BER

As Fig. 5.4 shown, poisson noise BER model predicts more accurate than Gaussian noise BER model as noise count rate low as 140 Hz. When the detected photon number is below 15 per bit, experiment results fit predicted results very well, but clearly deviate over 15 photons per bit. This is explained by the shot noise, which is positive to the receive photon number. The current flow from the filter output, induced by the incident optical wave, is

$$i = i_s + i_N, \qquad i_s = \frac{\eta e P_s}{hv} \tag{5.1}$$

where, i_N is detector noise and i_s is the signal current. The random shot noise current i_N at the output of the filter is assumed to be a zero mean so the total noise power is defined

by

$$\sigma_N^2 =< i^2 > - < i >^2 =< i_N^2 >, \tag{5.2}$$

where the mean-square noise value is [**?**]

$$< i_N^2 >= 2eBi_s = \frac{2\eta e^2 BP_s}{hv} \tag{5.3}$$

Here P_s is the signal power in watts, η is the detector quantum efficiency in electrons, e is the electric charge in coulombs, h is Plancks constant ($h = 6.63 * 10^{-34}$, and v is optical frequency in hertz. Hence, the detector current noise power is proportional to detected photon number.

5.3.3 Neighbor Discovery Test Results

The results obtained in the previous two experiments, allowed us to discover the best configuration to use during the testing of our protocols. By best configuration we mean the distances and pointing angles that achieved the lowest path loss and BER. The configuration consisted of having a transmitter pointing angle of 50° and a receiver pointing angle of 40°. Other configurations could be used, but these pointing angles allowed us to establishing a NLOS link for communication. The nodes were also set apart by a distance of half a meter. The nodes were then allowed to run the neighbor discovery and MAC script. The images that are presented were captured during the operation of the nodes. A number of images have letters and numbers in their top portion. These letters and numbers simply represent the data that was received.

Figure 5.5 shows the initial states of the two nodes. As we can see, both nodes begin with empty Connection, Receiving Node, and Termination Tables. The top image

shows that one of the nodes (node 1) begins by being in a Standby state where it simply listens to the medium and decodes any information it receives. This node can be considered as the neighbor node. From the bottom image, we are able to see that the other node (node 2) was selected as the leader and has 55 initiated the neighbor discovery process. The leader sent a total of 5 request packets, one in every direction. The leader then entered the Wait for Feedback state where it waits to receive a response from its neighbor.

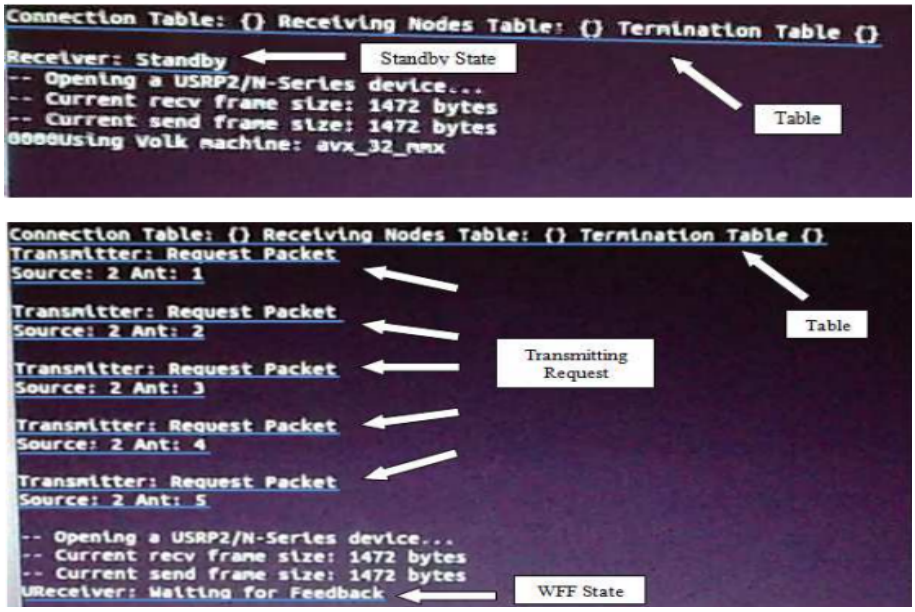

Figure 5.5: Initial states of nodes during neighbor discovery.

From the top image of Figure 5.6, we can see that the neighbor node that was in the Standby state received the request packet. The request packet contained the address of the leader (address 2) and the direction that it used to sent it (direction 5). The node then replied with a feedback packet containing its address (address 1) and the direction that leader initially used to send the request packet (direction 5). The neighbor node then

returned to the standby state.

Figure 5.6: Showing a node receiving a request packet (top) and a feedback packet (bottom).

The bottom image allows us to see that the leader was able to successfully receive the feedback packet. The leader proceeds to construct its Connection, Receiving Nodes, and Termination Tables. The Termination Table was updated, and shows that the node served as the leader once. The leader then selects its successor (node 1), and transmits a notify packet allowing the node to become aware that it was selected as the leader. The node then proceeds to enter the standby state.

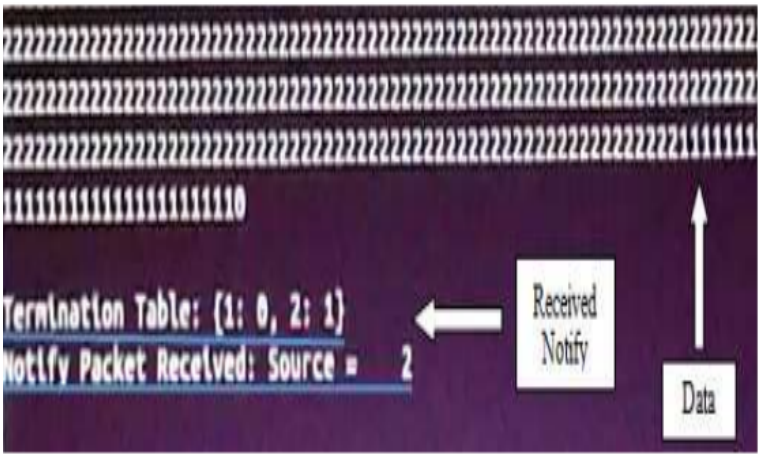

Figure 5.7: Image of a node receiving a notify packet.

Using Figure 5.7, we can now see that the neighbor has received the notify packet and the Termination Table. The node then proceeds to continue the neighbor discovery process. The process continues until both nodes have marked themselves as being finished with the neighbor discovery process. At this point, the process terminates, and the MAC begins its operation.

5.3.4 MAC Test Results

After the neighbor discovery results were obtained, tests were performed on the MAC to better understand its performance. During the tests, the nodes were assumed to have their neighborhood information. The nodes contained the addresses and the directions they could use to communicate with their neighbors. The nodes were then allowed to run the MAC script.

Figure 5.8 gives us the initial states of the two nodes during the MAC test. From

the images, we are able to see that both nodes have Connection and Receiving Nodes Tables containing their neighborhood information. The top image allows us to see that node 2 is in the idle state. The node is able to simply listen to the medium and decode any information it receives. The bottom image shows that the node 1 has information to send. Node 1 has proceeded to send a CTS message, making its neighbor aware that it has pending data to send. After node 1 has finished sending the CTS message, node 1 enters the Wait for CTS state where it waits to receive a response.

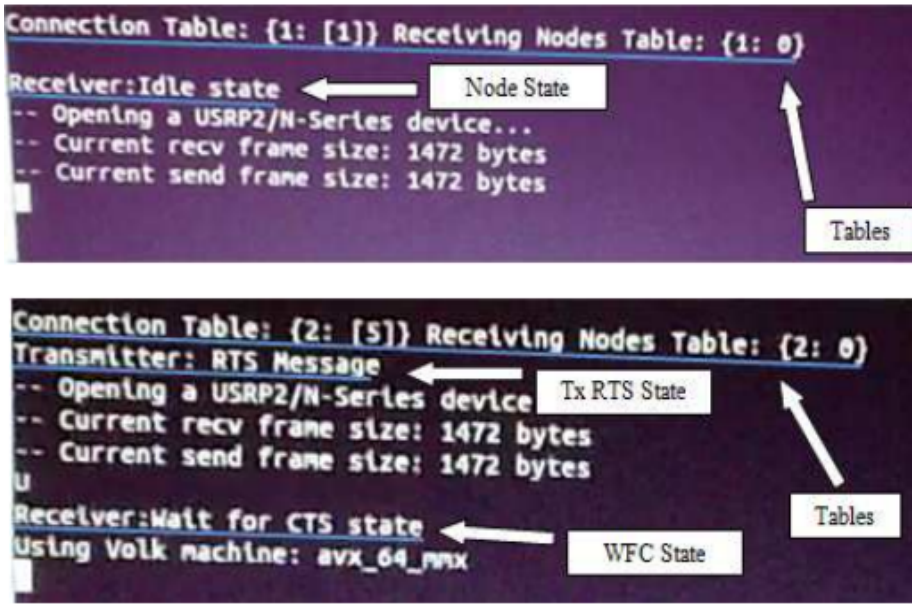

Figure 5.8: Initial states of the node running the MAC script.

Using fig. 5.9, we are able to see that node 2, initially in the Idle state, was able to receive the RTS message from node 1. The node was also able to conclude that the RTS message was addressed to it. Node 2 proceeds to respond by transmitting a CTS message. Once it has finished transmitting, it enters the Wait for Data state where it waits to receive

the information. Figure 5.9 also allows us to see that a CTS message was successfully received by node 1. We are able to see that the CTS message was transmitted by node 2 and was addressed to node 1. Node 1 responds by transmitting the pending data. Once node 1 has finished transmitting the data, it enters the Idle state.

Figure 5.9: Image of nodes receiving an RTS (top) and CTS (bottom) message.

Lastly, fig. 5.10 shows node 2 receiving the data from node 1. The information was sent using direction 1. Node 2 is now able to return to the Idle state.

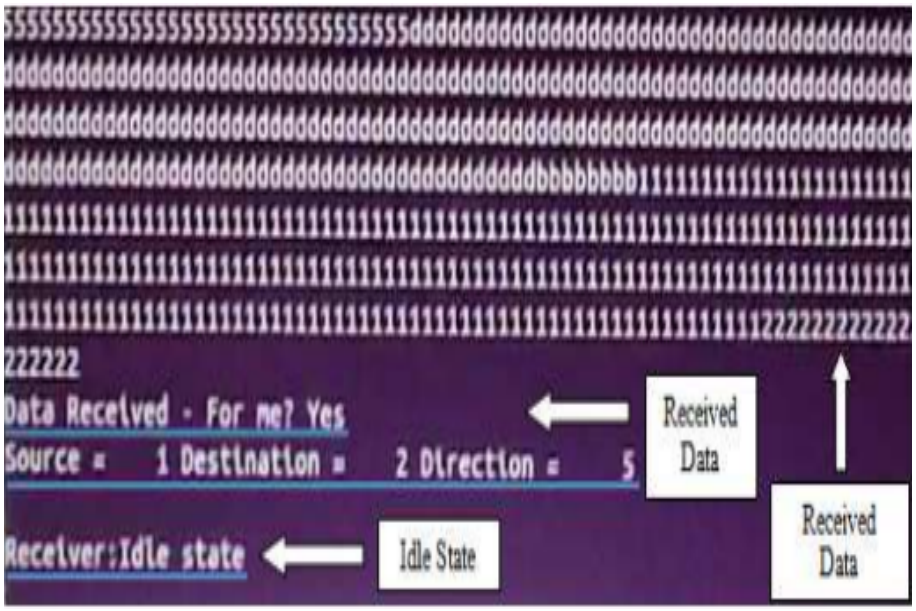

Figure 5.10: Showing a node receiving data.

5.4 Summary

Based on UV USRP system, we compared practical system performance to three previous proposed path loss models and BER models. All discrepancies are analyzed, which are valuable for UV communication system design and proposal for new prediction model. What's more, We were also able to verify the basic operation of both our protocols. From the results, we are able to see that a node is able to react accordingly to the information it receives. The nodes were able to find each other during the neighbor discovery process. They were able to obtain the address of its neighbor and the direction it could use to communicate with it. Once a node contained this information, the MAC protocol was used to exchange information.

Chapter 6

Conclusions

We reported on several first-hand data collection experiments in which a variety of channel-sounding measurements were taken to characterize various aspects of long-distance NLOS UV communications. In particular, analyses of measurements of path loss, pulse broadening, and photon-count distributions were presented and compared with previously developed theoretical channel models. Using the experimental path loss measurements, we also considered the BER performance of a representative long-distance NLOS UV communication system.

Predictions from a Monte Carlo propagation model are in reasonable agreement with several of the experimental measurements, providing validation of this modeling approach. However, the path loss measurements do exhibit mismatch with this channel model, which generally under predicts the observed path loss. This mismatch might be attributable in part to tolerances in device specifications, but other possible sources of additional channel attenuation should be considered. For example, we presented path loss estimates incorpo-

rating turbulence-induced attenuation (as predicted by previously developed turbulence modeling) that exhibit reduced error with respect to the path loss measurements. However, model predictions of other turbulence effects, such as a log-normal distribution of received photon counts, do not appear to be supported by the experimental data, suggesting the need for model refinement.

Therefore, we then conducted a series of measurements to investigate NLOS U-V turbulence channel for the first time. The received-signal distributions and NLOS UV turbulence channel path losses were studied in terms of system geometry and turbulence strength. The comparison between experimental and simulated results provided the validation for the NLOS UV turbulence channel model based on MC method. Through field test data and simulation results, the received-signal energy is proved to follow LN distribution in NLOS scenarios when the pointing angles are low and the atmosphere is in weak-medium turbulence condition. In addition, we also prove that turbulence effect will induce extra path loss for NLOS UV communication. The special characteristic of NLOS UV channel was also observed and analyzed through experiment and simulation. Because of this special characteristic, the choice of system geometry becomes a trade off between the size of common volume and channel length. Those above experimental and simulated analysis is valuable to fundamentally understand the NLOS UV turbulence channel, which is an essential prerequisite to the design of a NLOS UV communication system.

Further open work in this area include the outdoor experiment and model verification under severe turbulence condition. Due to the special characteristic of NLOS UV turbulence channel, the choice of best system geometry is still an open research topic.

Bibliography

[1] D. M Reilly. Atmospheric optical communication in the middle ultaviolet. *M.S. Thesis, MIT, Cambridge*, 1976.

[2] M. R. Luettgen, J. H. Shapiro, and D. M. Reilly. Non-line-of-sight single-scatter propagation model. *J. Opt. Soc. Am*, A8:1964–1972, 1991.

[3] W. S. Ross and R. S. Kennedy. An investigation of atmospheric optically scattered non-light-of-sight communication links. *Army Research Office Project Report, Research Triangle Park, NC*, January 1980.

[4] J. J. Puschell and R. Bayse. High data rate ultraviolet communication systems for the tactical battlefield. pages 253–267, April 1990.

[5] Z. Xu and B. M. Sadler. Ultraviolet communications: potential and state-of-the-art. *IEEE Commun. Mag*, 46(5):67–73, 2008.

[6] G. Chen, Z. Xu, H. Ding, and B. M. Sadler. Path loss modeling and performance trade-off study for short-range non-line-of-sight ultraviolet communications. *Opt. Exp*, 17(5):3929–3940, 2009.

[7] H. Ding, G. Chen, A. K. Majumdar, B. M. Sadler, and Z. Xu. Modeling of non-line-of-sight ultraviolet scattering channels for communication. *IEEE J. Sel. Areas Commun*, 27(9):1535–1544, 2009.

[8] R. J. Drost, T. J. Moore, and B. M. Sadler. Monte-carlo-based multiple-scattering channel modeling for non-line-of-sight ultraviolet communications. *Proc. SPIE 8038, Atmospheric Propagation VIII, 803802*, 2011.

[9] G. Chen, R. J. Drost, B. M. Sadler, and L. Liao. Long-distance ultraviolet scattering channel measurements: analog vs. digital approaches. *in Conf. on Lasers and Electro-Optics*, 88, 2013.

[10] Q. He, B. M. Sadler, and Z. Xu. Modulation and coding tradeoffs for non-line-of-sight ultraviolet communications. *in Proc. SPIE*, 7464, 2009.

[11] M. Noshad, M. Brandt-Pearce, and S. G. Wilson. Nlos uv communications using m-ary spectral-amplitude-coding. *IEEE Trans.Commun*, 61(4):1544–1553, 2013.

[12] Y. Li, L. Wang, Z. Xu, and S. V. Krishnamurthy. Neighbor discovery for ultraviolet ad hoc networks. *IEEE J. Sel. Areas Commun*, 29(10):2002–2011, 2011.

[13] L. Wang, Y. Li, and Z. Xu. On connectivity of wireless ultraviolet networks. *J. Opt. Soc. Am. A,*, 29(10):1970–1978, 2011.

[14] A. Vavoulas, H. G. Sandalidis, and D. Varoutas. Connectivity issues for ultraviolet uv-c networks. *J. Opt. Commun. Netw.*, 3(3):199–205, 2011.

[15] G. A. Shaw, A. M. Siegel, and M. L. Nischan. Demonstration system and applications for compact wireless ultraviolet communications. *Proc. SPIE*, 5071:241–252, 2003.

[16] L. Liao, B. M. Sadler, and G. Chen. Gps synchronized uv usrp communication system. *Proc. SPIE*, 8874(887409).

[17] H. Ding, G. Chen, A. K. Majumdar, B. M. Sadler, and Z. Xu. Turbulence modeling for non-line-of-sight ultraviolet scattering channels. *in Proc. SPIE*, 8038(80380J).

[18] Y. Zuo, H. Xiao, J. Wu, X. Hong, and J. Lin. Effect of atmospheric turbulence on non-line-of-sight ultraviolet communications. *in IEEE 23rd Int. Symp. on Personal Indoor and Mobile Radio Communications*, pages 1682–1686, 2012.

[19] H. Xiao, Y. Zuo, C. Fan, C. Wu, and J. Wu. Non-line-of-sight ultraviolet channel parameters estimation in turbulence atmosphere. *in Asia Communications and Photonics Conf, AF3G*, 5, 2012.

[20] G. Chen, F. Abou-Galal, Z. Xu, and B. M. Sadler. Experimental evaluation of led-based solar blind nlos communication links. *Optics Express*, 16:15059–15068, 2008.

[21] D. M. Reilly and C. Warde. Temporal characteristics of singlescatter radiation. *J. Opt. Soc. Am*, 19(3):464–470, May 1979.

[22] Z. Xu, H. Ding, B. M. Sadler, and G. Chen. Analytical performance study of solar blind non-line-of-sight ultraviolet short-range communication links. *Optics Letters*, 33(16):1860–1862, August 2008.

[23] Q. He, Z. Xu, and B. M. Sadler. Performance of short-range non-line-of-sight led-based ultraviolet communication receivers. *Optics Express*, 18:12226–12238, 2010.

[24] G. A. Shaw, A. M. Siegel, and J. Model. Extending the range and performance of non-line-of-sight ultraviolet communication links. volume 6231, pages 62310C–162310C–12, 2006.

[25] R. J. Drost, T. J. Moore, and B. M. Sadler. Uv communications channel modeling incorporating multiple scattering interactions. *J. Opt. Soc. Am. A*, 28:686695, 2011.

[26] R. J. Drost, P. L. Yu, G. Chen, and B. M. Sadler. Receiver dead time in non-line-of-sight ultraviolet communications. *Proc. SPIE*, 9114, 2014, 91140Q.

[27] R. J. Drost, B. M. Sadler, and G. Chen. Dead time effects in non-line-of-sight ultraviolet communications. *Optics Express*, 23:15748–15761, 2015.

[28] A. S. Zachor. Aureole radiance field about a source in a scattering-absorbing medium. *Appl. Opt.*, 17(12):1911–1922, June 1978.

[29] G. Chen, Z. Xu, and B. M. Sadler. Experimental demonstration of ultraviolet pulse broadening in short-range non-line-of-sight communication channels. *Opt. Exp.*, 18(10):10500–10509, May 2010.

[30] D. L. Hutt and D.H. Tofsted. Effect of atmospheric turbulence on propagation of ultraviolet radiation. *Optical & Laser Technology*, 32(1), Feb. 2000.

[31] A. Tunick, N. Tikhonov, M. Vorontsov, and G. Carhart. Characterization of optical turbulence (*Cn2*) data measured at the arl_a lot facility. *ARL, Adelphi, MD*, ARL-MR-625, Sept. 2005.

[32] L. Dordová and O. Wilfert. Laser beam attenuation determined by the method of available optical power in turbulent atmosphere. *J. Telecommun. Inform. Technol.*, (2):53–57, 2009.

[33] M. Al Naboulsi, H. Sizun, and F. de Fornel. Propagation of optical and infrared waves in the atmosphere. *Proc. of the XXVIIIth General Assembly of International Union Radio Science, New Delhi, India*, 2005.

[34] P. Wang and Z. Xu. Characteristics of ultraviolet scattering and turbulent channels. *Opt. Lett.*, 38(15):2773–2775, Aug. 2013.

[35] G. Chen, L. Liao, Z. Li, R. Drost, and B. Sadler. Experimental and simulated evaluation of long distance nlos uv communication. *CSNDSP*, pages 904–909, 2014.

[36] Larry C. Andrews and Ronald L. Phillips. *Laser Beam Propagation through Random Media, Second Edition*, volume PM152. Sep, 2005.

[37] G. Chen, Z. Xu, and B. M. Sadler. Experimental demonstration of non-line-of-sight ultraviolet communication channel characteristics. volume 781407, 2010.

[38] D. Kedar and S. Arnon. Non-line-of-sight optical wireless sensor network operating in multiscattering channel. *Appl. Opt.*, 45(33):8454–8461, 2006, Nov.

[39] G. Chen, F. Abou-Galala, Z. Xu, and B. M. Sadler. Experimental evaluation of led-based solar blind nlos communication links. *Opt. Exp.*, 16(19):15059–15068, 2008, Sept.

[40] H. Xiao, Y. Zuo, J. Wu, H. Guo, and J. Lin. Non-line-ofsight ultraviolet single-scatter propagation model. *Opt. Exp.*, 19(18):1786417875, 2011, Aug.

[41] Y. Zuo, H. Xiao, J. Wu, and J. Lin. A singlescatter path loss model for non-line-of-sight ultraviolet channels. *Opt. Exp.*, 20(9):1035910369, 2012, April.

[42] R. Qiang, S. Zhao, X. Wang, and Y. Liu. Influence of high atmosphere turbulence on scintillationin non-line-of-sight-ultraviolet channel. *Semiconductor Optoelectronics*, 35(4):677–681, 2005.

[43] S Karp, R. M. Gagliardi, Moran, S. E., and L. B. Stotts. *Optical Channels: Fibers, Clouds, Water, and the Atmosphere*. 1988.

[44] D. Moriarty and B. Hombs. System design of tactical communications with solar blind ultraviolet non line-of-sight systems. *systems,"Military Communications Conf.*, 2009.